

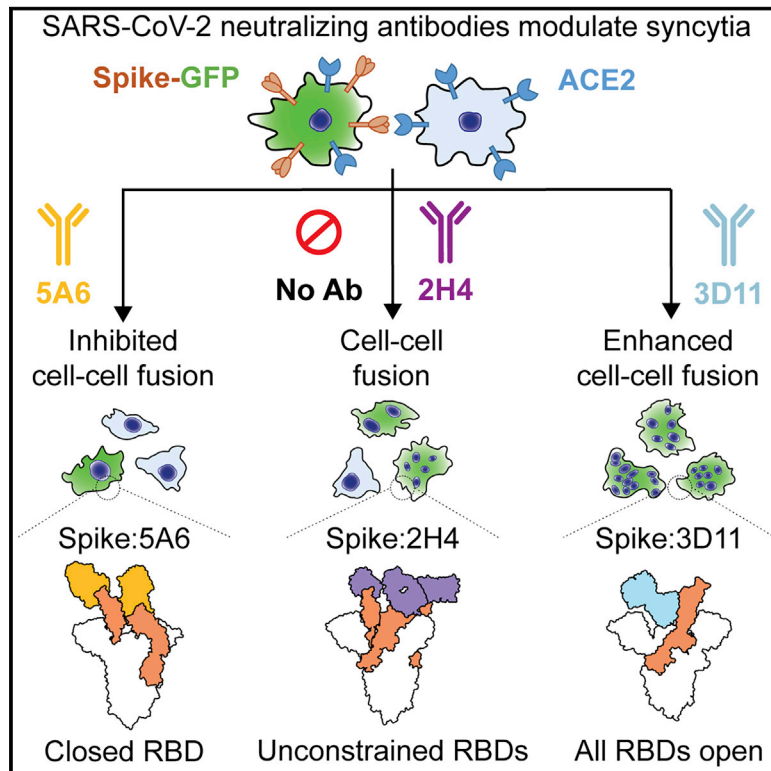


Since January 2020 Elsevier has created a COVID-19 resource centre with free information in English and Mandarin on the novel coronavirus COVID-19. The COVID-19 resource centre is hosted on Elsevier Connect, the company's public news and information website.

Elsevier hereby grants permission to make all its COVID-19-related research that is available on the COVID-19 resource centre - including this research content - immediately available in PubMed Central and other publicly funded repositories, such as the WHO COVID database with rights for unrestricted research re-use and analyses in any form or by any means with acknowledgement of the original source. These permissions are granted for free by Elsevier for as long as the COVID-19 resource centre remains active.

Structural insight into SARS-CoV-2 neutralizing antibodies and modulation of syncytia

Graphical abstract



Authors

Daniel Asarnow, Bei Wang, Wen-Hsin Lee, ..., Yifan Cheng, Charles S. Craik, Cheng-I Wang

Correspondence

aashish.manglik@ucsf.edu (A.M.), ycheng@ucsf.edu (Y.C.), charles.craik@ucsf.edu (C.S.C.), wang_chengi@immunol.a-star.edu.sg (C.-I.W.)

In brief

A series of antibodies against SARS-CoV-2 that potentially block binding to the host receptor ACE2 are found to enhance or inhibit virus Spike-mediated membrane fusion and formation of syncytia, a sign of tissue damage in individuals with COVID-19.

Highlights

- The affinity of neutralizing antibodies does not always predict antiviral potency
- Receptor-blocking antibodies can inhibit or enhance syncytium formation
- Cryo-EM reveals one antibody inhibits syncytia by trapping the pre-fusion Spike
- Another antibody acts as an allosteric effector that promotes syncytium formation



Article

Structural insight into SARS-CoV-2 neutralizing antibodies and modulation of syncytia

Daniel Asarnow,^{1,3,13} Bei Wang,^{2,13} Wen-Hsin Lee,^{2,14} Yuanyu Hu,^{2,14} Ching-Wen Huang,^{2,14} Bryan Faust,^{1,3,14} Patricia Miang Lon Ng,^{2,14} Eve Zi Xian Ngoh,^{2,14} Markus Bohn,^{3,4,14} David Bulkley,^{1,3,14} Andrés Pizzorno,^{5,14} Beatrice Ary,^{3,4} Hwee Ching Tan,² Chia Yin Lee,² Rabiatul Adawiyah Minhat,² Olivier Terrier,⁵ Mun Kuen Soh,² Frannie Jiuyi Teo,² Yvonne Yee Chin Yeap,² Shirley Gek Kheng Seah,⁶ Conrad En Zuo Chan,⁶ Emily Connelly,⁴ Nicholas J. Young,⁴ Sebastian Maurer-Stroh,^{7,8,9} Laurent Renia,^{2,8} Brendon John Hanson,⁶ Manuel Rosa-Calatrava,^{5,10} Aashish Manglik,^{3,4,11,*} Yifan Cheng,^{1,3,12,*} Charles S. Craik,^{3,4,*} and Cheng-I Wang^{2,15,*}

¹Department of Biochemistry and Biophysics, University of California, San Francisco (UCSF) School of Medicine, San Francisco, CA, USA

²Singapore Immunology Network, Agency for Science, Technology and Research (A*STAR), 8A Biomedical Grove, Immunos, Singapore 138648, Singapore

³QBI COVID-19 Research Group (QCRG), San Francisco, CA, USA

⁴Department of Pharmaceutical Chemistry, University of California, San Francisco (UCSF), San Francisco, CA, USA

⁵CIRI, Centre International de Recherche en Infectiologie (Team VirPath), Université de Lyon, INSERM U1111, Université Claude Bernard Lyon 1, CNRS, UMR5308, ENS de Lyon, 69007 Lyon, France

⁶Biological Defence Program, DSO National Laboratories, 27 Medical Drive, Singapore 117510, Singapore

⁷Bioinformatics Institute, Agency for Science, Technology and Research (A*STAR), 30 Biopolis Street, Matrix, Singapore 138671, Singapore

⁸Infectious Diseases Laboratories (ID Labs), Agency for Science, Technology and Research (A*STAR), 8A Biomedical Grove, Immunos, Singapore 138648, Singapore

⁹Department of Biological Sciences, Faculty of Science, National University of Singapore, Singapore 117558, Singapore

¹⁰VirNext, Faculté de Médecine RTH Laennec, Université Claude Bernard Lyon 1, Université de Lyon, Lyon, France

¹¹Department of Anesthesia and Perioperative Care, UCSF, San Francisco, CA, USA

¹²Howard Hughes Medical Institute, UCSF, San Francisco, CA, USA

¹³These authors contributed equally

¹⁴These authors contributed equally

¹⁵Lead contact

*Correspondence: aashish.manglik@ucsf.edu (A.M.), ycheng@ucsf.edu (Y.C.), charles.craik@ucsf.edu (C.S.C.), wang_chengi@immunos.a-star.edu.sg (C.-I.W.)

<https://doi.org/10.1016/j.cell.2021.04.033>

SUMMARY

Infection with severe acute respiratory syndrome coronavirus 2 (SARS-CoV-2) is initiated by binding of the viral Spike protein to host receptor angiotensin-converting enzyme 2 (ACE2), followed by fusion of viral and host membranes. Although antibodies that block this interaction are in emergency use as early coronavirus disease 2019 (COVID-19) therapies, the precise determinants of neutralization potency remain unknown. We discovered a series of antibodies that potently block ACE2 binding but exhibit divergent neutralization efficacy against the live virus. Strikingly, these neutralizing antibodies can inhibit or enhance Spike-mediated membrane fusion and formation of syncytia, which are associated with chronic tissue damage in individuals with COVID-19. As revealed by cryoelectron microscopy, multiple structures of Spike-antibody complexes have distinct binding modes that not only block ACE2 binding but also alter the Spike protein conformational cycle triggered by ACE2 binding. We show that stabilization of different Spike conformations leads to modulation of Spike-mediated membrane fusion with profound implications for COVID-19 pathology and immunity.

INTRODUCTION

The first step of infection with coronaviruses such as severe acute respiratory syndrome coronavirus (SARS-CoV) and severe acute respiratory syndrome coronavirus 2 (SARS-CoV-2) is binding of a Spike protein on the virion to a specific receptor in the membrane of a host cell (Tortorici and Veesler, 2019). The virus enters cells by fusion of the viral envelope with cellular plasma membranes and, alternatively, by endocytosis and subsequent

fusion of the viral envelope with endosomal membranes. The SARS-CoV-2 Spike protein, similar to that of other CoVs, comprises two subunits, S1 and S2, and is responsible for target recognition and mediating virus entry (Tortorici and Veesler, 2019). Upon binding to the host cell receptor through the receptor binding domain (RBD) at the tip of the S1 subunit, the Spike protein undergoes dramatic conformational changes and proteolytic processing. Further shedding of the S1 subunit exposes the S2 subunit fusion peptide, which inserts into the host cell



membrane and induces viral fusion (Benton et al., 2020). SARS-CoV-2 and SARS-CoV use angiotensin-converting enzyme 2 (ACE2) as the entry receptor to infect host cells (Hoffmann et al., 2020; Walls et al., 2020; Zhou et al., 2020). The RBD binds to ACE2 via the receptor binding motif (RBM), a small patch made up of about 20 amino acids (Lan et al., 2020; Tai et al., 2020).

In addition to mediating virus entry, excess Spike protein in the membranes of CoV-infected cells drives neighboring cells expressing ACE2 to fuse and form syncytia (multinucleated giant cells) through a pH-independent mechanism (Musarrat et al., 2020; Shulla et al., 2011). Syncytia are associated with lung tissue damage in SARS-CoV and Middle East respiratory syndrome coronavirus (MERS-CoV) infection and have been observed widely in autopsies of individuals afflicted with severe coronavirus disease 2019 (COVID-19) (Bussani et al., 2020; Xu et al., 2020). Preliminary reports also implicate syncytia in chronic cardiovascular injury because of COVID-19 (Schneider et al., 2020).

A common therapeutic strategy against COVID-19 and other CoV-related illnesses is blocking the RBD/ACE2 interaction with antibodies, nanobodies, or soluble ACE2 as a decoy (Zhou and Zhao, 2020). Since the first report of COVID-19, many SARS-CoV-2 neutralizing monoclonal antibodies (NAbs) have been discovered in immunized animals (Hansen et al., 2020; Wang et al., 2020; Wrapp et al., 2020a) and COVID-19 convalescent individuals (Brouwer et al., 2020; Cao et al., 2020; Chi et al., 2020; Hansen et al., 2020; Ju et al., 2020; Lou et al., 2020; Rogers et al., 2020; Shi et al., 2020; Wan et al., 2020; Wu et al., 2020). Most SARS-CoV-2 NAbs recognize epitopes within the ACE2 binding site, imposing direct competition between the virus-ACE2 interaction (Brouwer et al., 2020; Cao et al., 2020; Hansen et al., 2020; Shi et al., 2020, 2020; Wu et al., 2020), whereas others bind outside the RBM (Hansen et al., 2020; Pinto et al., 2020; Wang et al., 2020) or even the RBD (Brouwer et al., 2020; Chi et al., 2020). A number of NAbs in advanced clinical trials have already been used as experimental treatments for COVID-19 (Hansen et al., 2020), with promising efficacy in individuals with early-stage infection. Competitive inhibition of receptor binding, denaturation of native Spike conformations (Huo et al., 2020), and pre-fusion trapping (Wang et al., 2020) may contribute to neutralization, but the molecular mechanisms governing the neutralization potency of NAbs remain poorly understood, and it is unknown whether receptor-blocking NAbs can also influence Spike-mediated cell-cell fusion and syncytium formation.

Neutralizing antibodies against pathogens can also be isolated by *in vitro* selection from highly diverse combinatorial human libraries (Frenzel et al., 2017; Lu et al., 2020; Vaughan et al., 1998) and may be distinct from those found with natural infection or immunization (Saphire et al., 2018). We screened a naive combinatorial human antibody fragment (Fab) library for antibodies that target the SARS-CoV-2 Spike protein RBD and competitively block ACE2 binding. We discovered a series of antibodies that exhibit effective receptor blockade but have strikingly different neutralization potencies against SARS-CoV-2. Taking these antibodies as mechanistic probes, we show that bivalent binding and receptor blockade are not the sole determi-

nants of potent neutralization. In addition to blocking ACE2, these antibodies inhibit or enhance syncytium formation in Vero E6 cells, suggesting that potentiation of cell-cell fusion by antibodies may compromise the effectiveness of virus neutralization in treatment of severe COVID-19. One potentially neutralizing and potentially therapeutic antibody, designated 5A6, uniquely inhibits cell-cell fusion and syncytium formation and blocks receptor binding. High-resolution cryoelectron microscopy (cryo-EM) structures of multiple Spike-antibody complexes provide insight into determinants of viral neutralization potency and reveal that 5A6 recognizes a cryptic quaternary epitope that conveys receptor blockade and inhibits syncytia by trapping the pre-fusion state.

RESULTS

Isolation of SARS-CoV-2 receptor-blocking antibodies from a naive human library

We identified six antibodies that block the RBD/ACE2 interaction with nanomolar EC₅₀ (half maximal effective concentration) values by phage display of a naive combinatorial human Fab library comprising 3×10^{10} random heavy and light immunoglobulin G (IgG) chain pairs drawn from 22 healthy donors (Goh et al., 2014; Figure 1A; Figure S1A). Their germlines and degree of hypermutation are given in Table S1. Although the source Fabs had moderate intrinsic affinities for immobilized RBD, as high as 1.6 nM for 3D11 and 7.6 nM for 5A6, clones reformatted as IgGs showed subpicomolar to picomolar binding avidity (Figure 1B; Figures S1B–S1D). Biolayer interferometry (BLI) of free Fabs and their equivalent IgGs indicates that the greatly enhanced binding of the IgGs is primarily due to slower dissociation, likely because of bivalent binding of both Fab arms to their epitopes (Figure 1C; Table S2). Stepwise binding BLI assays show that Fabs 5A6 and 3D11 have non-overlapping footprints on the RBD, whereas 5A6 shares at least partially overlapping epitopes with the other four antibodies (Figure 1D).

SARS-CoV-2 neutralization by receptor-blocking antibodies

We evaluated the six receptor-blocking antibodies for neutralizing activity against SARS-CoV-2 pseudovirus in Chinese hamster ovary (CHO)-ACE2 cells with a luciferase reporter (Figure 2A) and against live SARS-CoV-2 (Young et al., 2020) in Vero E6 cells by cell viability (Figure 2B). The antibodies neutralize the pseudovirus with IC₅₀ values ranging from 75.5–428.3 ng/mL, but although neutralization of the live virus is 11- to 20-fold less potent for other antibodies, 5A6 retains similar potency with an IC₅₀ (half maximal inhibitory concentration) value of 140.7 ng/mL (<2-fold weaker). We speculate that this difference in neutralization potency in live virus and pseudovirus assays is most likely due to the non-replicating nature of pseudoviruses, which are more sensitive to blockade of virus entry. We validated live virus neutralization of a subset of antibodies (2H4, 3D11, and 5A6) using qRT-PCR to quantify virus replication (Figure S2A) and observed similar trends as obtained from cell viability assays (Figure 2B). To more accurately assess the therapeutic potential of 5A6, we studied its neutralizing potency in SARS-CoV-2 infection of human airway epithelium (HAE) (Pizzorno et al., 2020).

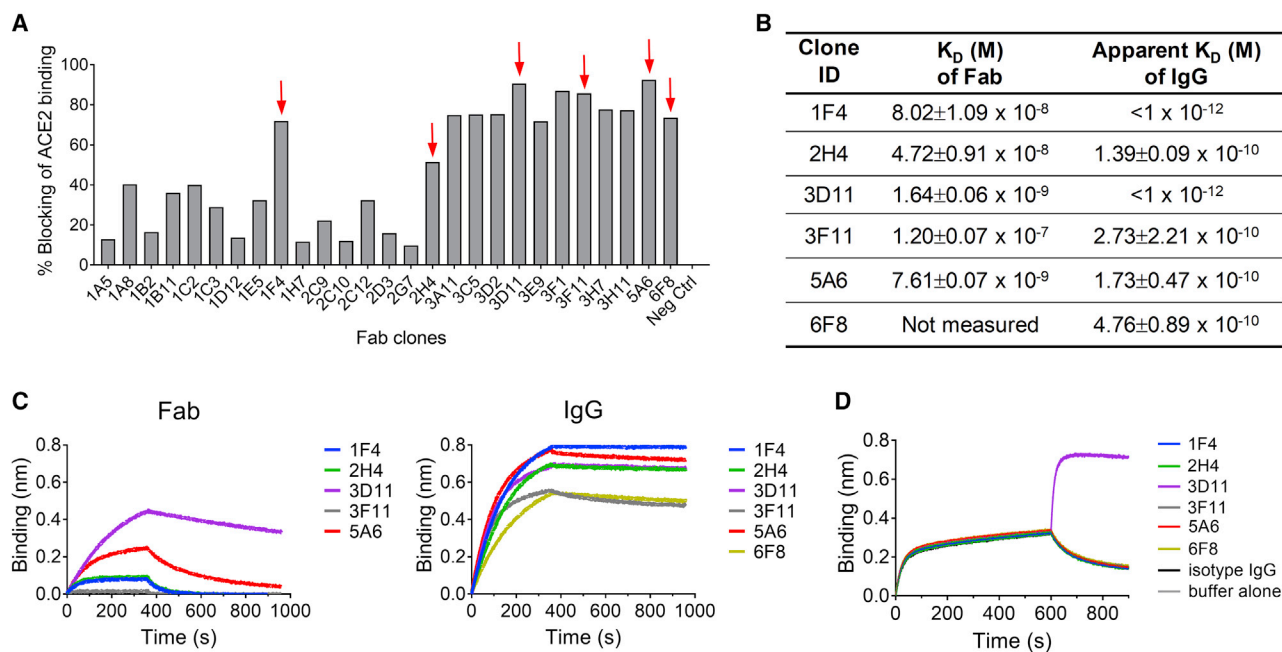


Figure 1. Isolation of SARS-CoV-2 receptor-blocking antibodies from a naive human library

(A) Blocking of ACE2/RBD (SARS-CoV-2) interactions by 27 Fab clones, tested by competition ELISA. The samples used in the assays were unpurified Fabs from bacterial supernatant; hence, the percentages of blocking were not indicative of their true potency. Red arrows indicate the 6 clones in subsequent studies. (B) K_D of Fabs based on 1:1 Langmuir fitting and apparent K_D of IgGs based on 1:2 bivalent analyte fitting of BLI sensorgrams for immobilized Fc-RBD. Values are the mean and standard deviation of two independent experiments.

(C) Binding and dissociation of Fabs and IgGs to and from immobilized Fc-RBD by BLI. The concentration of Fabs and IgGs shown is 12.5 nM.

(D) Epitope binning of 5A6 by BLI analysis. 5A6 is immobilized as the ligand. Tagless RBD is introduced as the first analyte. The second antibody is introduced as the second analyte. As controls, buffer alone, an isotype IgG, and 5A6 IgG were included as the second analyte.

See also [Figure S1](#) and [Tables S1](#) and [S2](#).

SARS-CoV-2 replication in HAE was reduced 1,000-fold by 5A6 at 75 ng/mL and 10,000-fold at 150 ng/mL, and 5A6 also helped maintain epithelium integrity (represented by *trans*-epithelial electrical resistance), supporting its activity in a physiologically relevant *in vitro* model ([Figure 2C](#)).

All IgGs effectively block ACE2-RBD binding, with IC_{50} values below 50 nM ([Figure S1A](#)). Therefore, the relative virus neutralization potencies of these antibodies cannot be ascribed to competitive receptor blocking alone. To interrogate other determinants of neutralization, we next compared the potency of each IgG antibody with its respective monomeric Fabs. A bivalent ACE2-Fc fusion protein was included as a reference for multivalent receptor blockade. All antibodies show dramatically increased potency against the live virus compared with the Fab, which is consistent with bivalent engagement of the Spike trimer by IgG compared with the monovalent Fab. The affinity or avidity for the RBD is generally predictive of virus neutralization IC_{50} values, with two striking exceptions ([Figure 2D](#); [Table S2](#)). Antibody 5A6 exhibits far greater viral neutralization potency than other antibodies with superior avidity. Conversely, 3D11 is among the least potent regarding virus neutralization despite displaying the strongest binding.

We wanted to find out whether the discrepancy could arise from the differences in the structural arrangement of IgGs bound to the RBDs of intact trimeric Spike on the virion. We used sur-

face plasmon resonance (SPR) to measure antibody binding to immobilized Spike trimers as opposed to the immobilized RBD ([Figures S2B–S2D](#); [Table S2](#)). Although the kinetics of binding to the trimer were largely similar, we noted that 5A6 IgG binds somewhat more tightly (3.6 \times) to the intact trimer than to the flexible Fc-RBD construct used for BLI, whereas 3D11 IgG binds much more weakly (18.7 \times) but still apparently bivalently, with 21.7 \times tighter binding than 3D11 Fab. To further investigate the relationship of the antibodies to intact Spike assemblies, we purified the SARS-CoV-2 pseudovirus by gradient centrifugation and immobilized the viral particles on ELISA plates. The higher optical signal at saturation in concentration-dependent binding curves reveals that 5A6 IgG likely packs with higher density on the virus surface than the other four tested IgG antibodies or 5A6 Fab ([Figure 2E](#)). It has been proposed that effective virus neutralization requires the antibody packing density to exceed a critical threshold ([Burton et al., 2001](#); [Dowd and Pierson, 2011](#); [Flamand et al., 1993](#)), and 5A6 may possess a unique binding mode that accommodates a denser structural arrangement on the virus surface. Notably, 3D11 IgG exhibits a similarly high signal at saturation but with lower affinity for the pseudoviral particles despite having a higher affinity than 5A6 for the immobilized RBD or Spike trimer ([Figure 2E](#); [Figure S2](#)). Finally, the 2H4 and 1F4 IgGs saturate the immobilized pseudovirus at 1/3 the density of 5A6 or 3D11 while neutralizing live virus slightly

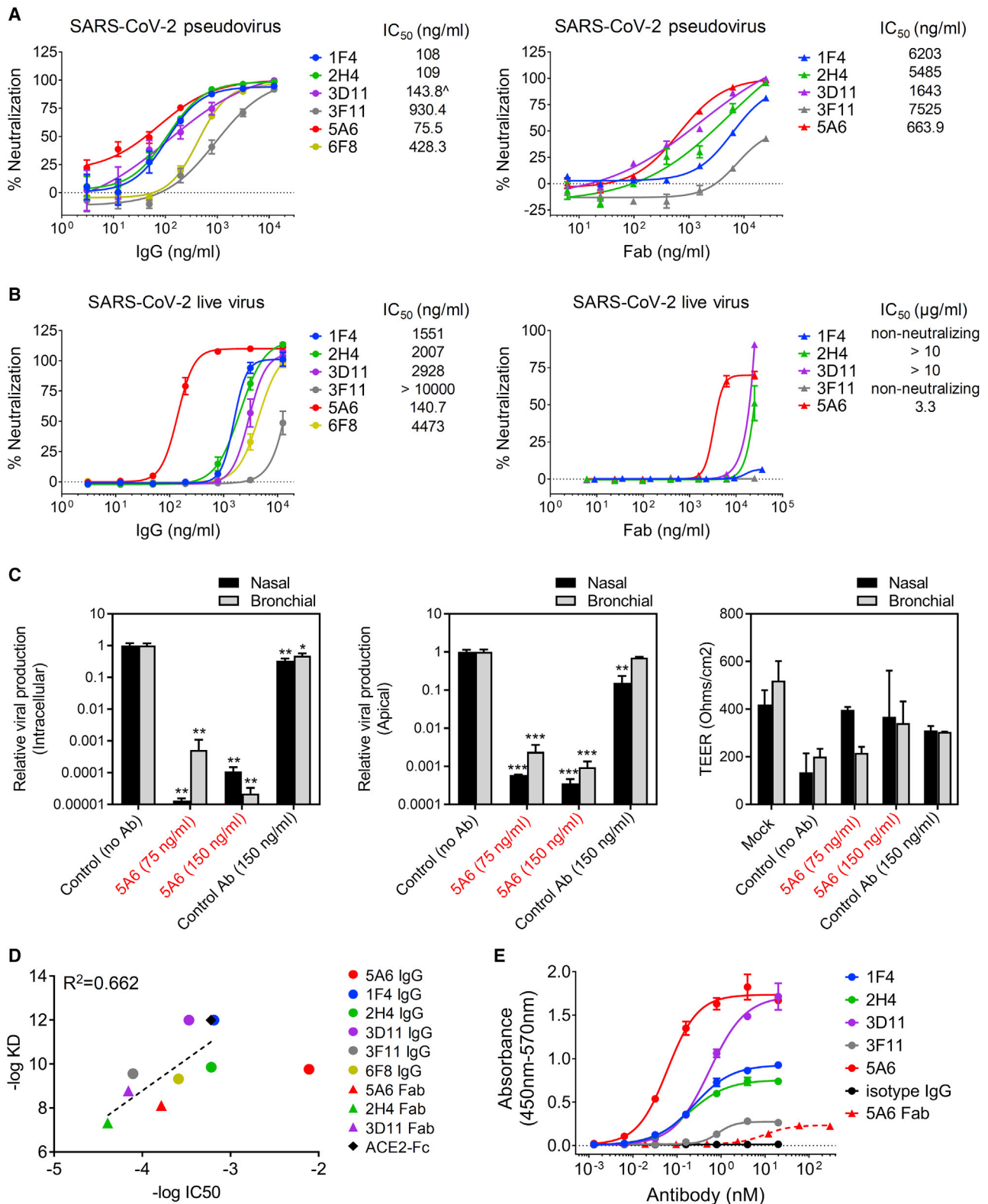


Figure 2. SARS-CoV-2 neutralization by receptor blocking antibodies.

(A) Infection of CHO-ACE2 cells by SARS-CoV-2 pseudovirus were determined in the presence of receptor-blocking IgGs (left panel) or Fabs (right panel). Luciferase activities in the CHO-ACE2 cells were measured, and the percent neutralization was calculated. Data are presented as mean ± SEM in triplicates and (legend continued on next page)

more effectively than 3D11. These results suggest at least three different classes of receptor-blocking antibodies with distinct structural relationships to RBDs on virus particles.

Neutralizing antibodies inhibit or enhance Spike-mediated cell fusion

It is widely appreciated that viral proteins often possess multiple critical functions. With receptor-blocking activity and avid binding eliminated as sole determinants of neutralization by prior experiments, we reasoned that 5A6 might interfere with additional functions of the SARS-CoV-2 Spike. The most prominent example is induction of fusion of infected cells with neighboring cells, leading to formation of syncytia (multinucleated giant cells), a phenomenon known to hasten disease progression in respiratory syncytial virus (McNamara and Smyth, 2002) and human immunodeficiency virus (Koot et al., 1993; Sylwester et al., 1997) and now observed widely in late-stage COVID-19 (Bussani et al., 2020). We therefore assessed whether antibodies discovered in our study inhibit Spike-mediated syncytium formation. To directly examine syncytium formation by Spike alone, we expressed the Spike protein with a C-terminal fluorescent tag in Vero E6 cells. Addition of trypsin as an exogenous Spike-processing enzyme resulted in cells with a diffuse fluorescent signal and multiple nuclei, indicative of syncytium formation (Figure 3A). We assayed the effect of receptor-blocking antibodies on this trypsin-induced cell-cell fusion using antibodies 2H4, 5A6, and 3D11, which represent different modes of virus neutralization. The 5A6 IgG has a dose-dependent inhibitory effect on syncytia (Figure 3B). In contrast 2H4 IgG has no significant effect. Surprisingly, 3D11 potentiates cell-cell fusion. Furthermore, 5A6 Fab also enhanced syncytial fusion, albeit weakly (Figures 3A and 3B). We conclude that 5A6 IgG directly inhibits Spike-mediated fusion, whereas other receptor-blocking antibodies fail to inhibit or even accelerate this process.

Structures of Spike-Fab complexes

The Spike trimer exists in equilibrium between the closed conformation, with all RBDs nestled closely around the S2 subunit, and “receptor-seeking” states featuring one or more open RBDs that become erect and disengage from the S2 subunit (Walls et al., 2020; Wrapp et al., 2020b; Yurkovetskiy et al., 2020). To provide structural insights into how antibodies targeting different RBD epi-

topes divergently modulate Spike protein function, we determined structures of the trimeric Spike protein alone (Figures S3A and S3B) and in complex with Fabs of 3D11 (Figures S3C and S3D), 2H4 (Figure S3E), and 5A6 (Figures S3F and S3G). Consistent with epitope binning and functional characterization, these Fabs explore different regions of the RBD surface, are compatible with different (open or closed) RBD states in the Spike trimer, and bind with distinct geometries relative to the RBD and ACE2 interface (Figure 4). This form of three-dimensional epitope mapping provides an atomic-level understanding of the determinants of virus inhibition.

2H4 is an orthosteric receptor-mimetic antibody

We determined multiple structures of 2H4 Fab bound to Spike with a resolution sufficient for unambiguously docking a model of 2H4 but precluding precise modeling of the epitope and complementarity-determining regions (CDRs) (Figure S3E). Three major conformational states were identified by 3D classification, revealing one, two, or three 2H4 Fabs bound to the Spike trimer. The receptor blocking activity of 2H4 is straightforward because it recognizes an epitope that overlaps much of the ACE2 interface (Figure 4A). Binding of the 2H4 Fab is compatible with both major RBD conformations, and the structures are drawn from an ensemble of quaternary states reminiscent of those that follow ACE2 binding and lead to S1 shedding and Spike-mediated membrane fusion (Benton et al., 2020; Figure 4B). The first of three predominant states features 2H4 bound to one open RBD, and the other two RBDs are closed. The second state adds a second copy of 2H4 on a closed RBD counterclockwise from the first. Density inspection and 3D variability analysis (3DVA) (Punjani and Fleet, 2021) reveal that the third RBD is primarily open, and a trajectory of opening states correlates with binding the second Fab (Video S2). The final state features three Fabs bound and a strictly open third RBD. This restricted ensemble arises because, when the bound RBD is closed, the Fab incurs clashes with the counterclockwise adjacent RBD that can only be relieved by opening of that RBD and N-terminal domain (NTD), even beyond the degree of opening in the triple ACE2 complex with three open RBDs (Benton et al., 2020; Figure 4C). These observations suggest that 2H4 directly blocks receptor binding but also acts as a receptor mimetic that admits the same cycle of Spike conformations as

are representative of two independent experiments. The IC_{50} was calculated by a variable-slope four-parameter non-linear regression model using GraphPad Prism 7 software or the Quest Graph IC_{50} Calculator from AAT Bioquest (<https://www.aatbio.com/tools/ic50-calculator>) with top and bottom constraints set at 100% and 0%, respectively.

(B) Infection of Vero E6 C1008 cells by SARS-CoV-2 live virus (isolated from a nasopharyngeal swab of an individual in Singapore) were determined in the presence of receptor-blocking IgGs (left panel) or Fabs (right panel). Infection-induced cytopathic effect was determined by detecting the amount of ATP present in the uninfected live cells from which the percent neutralization was calculated. Data are presented as mean \pm SEM in triplicates and are representative of two independent experiments. The IC_{50} was calculated by a variable-slope four-parameter non-linear regression model in GraphPad Prism 7 software. Pseudovirus and live virus neutralization assays were not performed for 6F8 Fab because of 6F8 IgG's low and similar potency to other clones.

(C) Evaluation of antiviral activity of 5A6 in a model of reconstituted human airway epithelium (HAE). Viral genome quantification was performed using qRT-PCR, and results are expressed in relative virus production (intracellular or apical) compared with the control. Bars represent the mean \pm SD in duplicates. *** $p < 0.001$, ** $p < 0.01$, and * $p < 0.05$ compared with the control (no Ab) by one-way ANOVA. The *trans*-epithelial electrical resistance (TEER in Ω/cm^2) was measured at 48 hrs (hours post-infection).

(D) Correlation curve of affinity/avidity for RBD and live virus neutralization potency (IC_{50}) of receptor-blocking IgG antibodies (circles), Fab antibodies (triangles), and ACE2-Fc (black diamond). The IC_{50} values were calculated using a four-parameter logistic regression model in the Quest Graph IC_{50} Calculator from AAT Bioquest.

(E) Binding of the IgG (solid lines, circles) and 5A6 Fab (dashed line, red triangle) to the purified SARS-CoV-2 pseudovirus. Data are presented as mean \pm SD in duplicates and are representative of two independent experiments.

See also Figure S2 and Table S2.

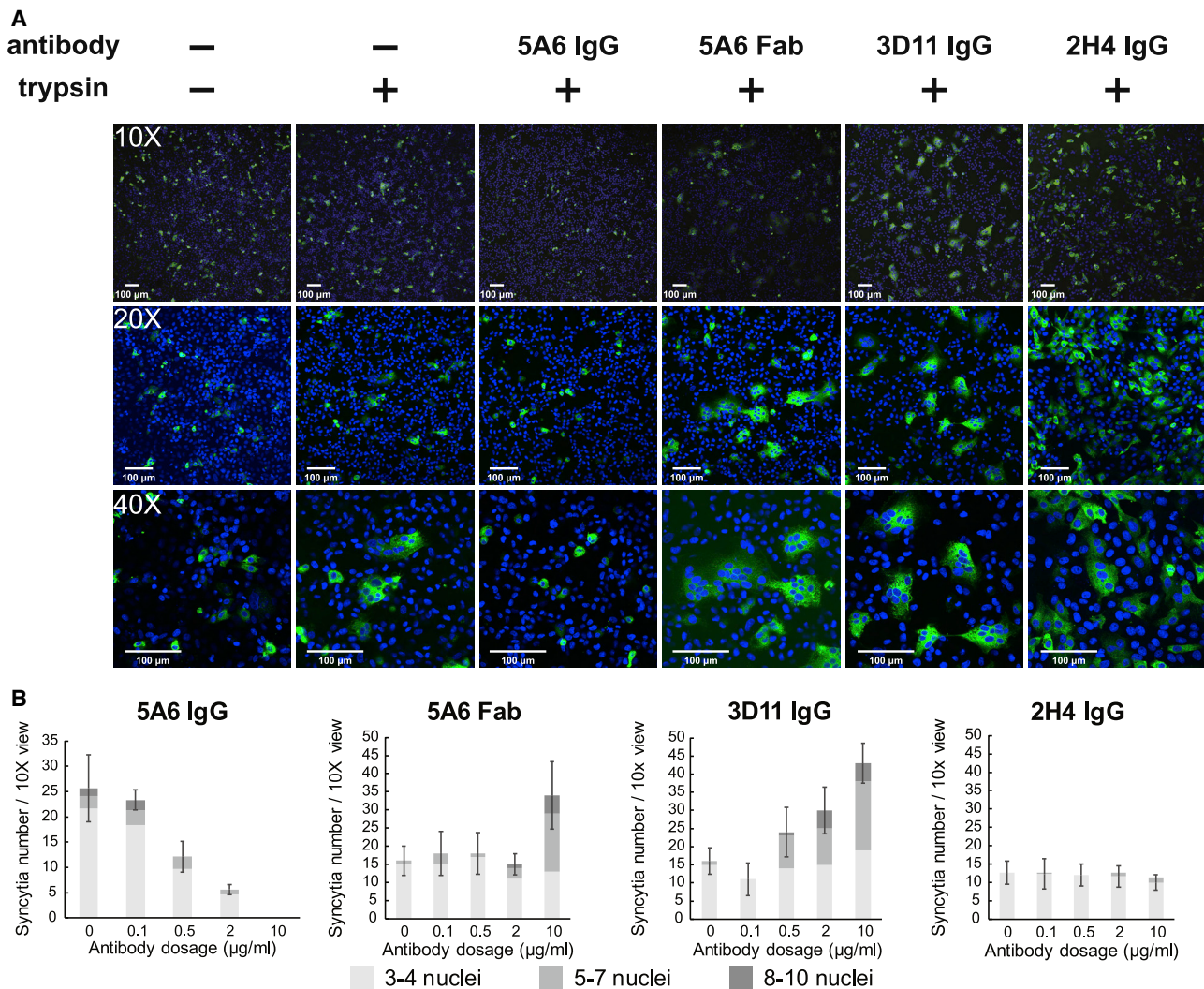


Figure 3. Anti-SARS-CoV-2 Spike RBD IgG antibodies affect trypsin-induced cell syncytium formation

Vero E6 cells were transfected with the furin recognition mutation of SARS-CoV-2 S-protein (R682RAR to A682AAR)-GFP. After 48 h, the cell culture medium was changed to DMEM (no serum), treated with antibodies or left untreated, and incubated for 1 h at 37°C. The cells were then treated with trypsin at 15 µg/mL for 2 h at 37°C or left untreated. Cells were fixed with 4% paraformaldehyde (PFA) and stained with DAPI.

(A) S protein-expressing Vero E6 cells treated with 5A6 IgG (20 µg/mL), 5A6 Fab (20 µg/mL), 3D11 IgG (20 µg/mL), and 2H4 IgG (10 µg/mL) in 10×, 20×, and 40× objective view. Images were taken using an Olympus confocal microscope.

(B) Dosage response of 5A6 IgG, 5A6 Fab, 3D11 IgG, and 2H4 IgG. S protein-expressing Vero E6 cells were treated with 0, 0.1, 0.5, 2, and 10 µg/mL of each antibody. For 5A6 IgG dosage response, 2×10^5 cells/sample were used for transfection. For 5A6 Fab, 2H4 IgG, and 3D11 IgG dosage response, 1.6×10^5 cells/sample were used for transfection. Data quantification was calculated on syncytium numbers and nuclei numbers in each syncytium. Data are presented as mean \pm SD of three images.

ACE2. A neutralizing antibody against SARS-CoV has also been reported to engage in orthosteric receptor mimicry (Walls et al., 2019), suggesting that activation of fusion-associated conformational changes may be an intrinsic consequence of direct receptor interface binding in betacoronaviruses.

3D11 allosterically blocks ACE2 binding and triggers Spike opening

The Spike:3D11 complex is relatively homogeneous, with only one major state (Figure 4D), and we determined its structure to ~ 3.0 -Å resolution (Figure S3C). All three RBDs are bound to

3D11 Fab in the open conformation, with the Fab making a right angle to the long axis of the RBD, via an epitope exposed only in the open state and outside of the RBM (Figure 4A). The epitope partly overlaps those of some other antibodies that bind outside of the RBM (Liu et al., 2020; Yuan et al., 2020) but is distinct from those (Barnes et al., 2020; Pinto et al., 2020) that bind freely to a closed RBD (Figure S4D). Clashes between 3D11 and Spike NTDs also prevent 3D11 binding to closed RBDs, indicating that 3D11 binds only to open RBDs. This restriction of binding to the subset of Spike conformations with open RBDs might account for lessened avidity of 3D11 IgG for the intact Spike trimer

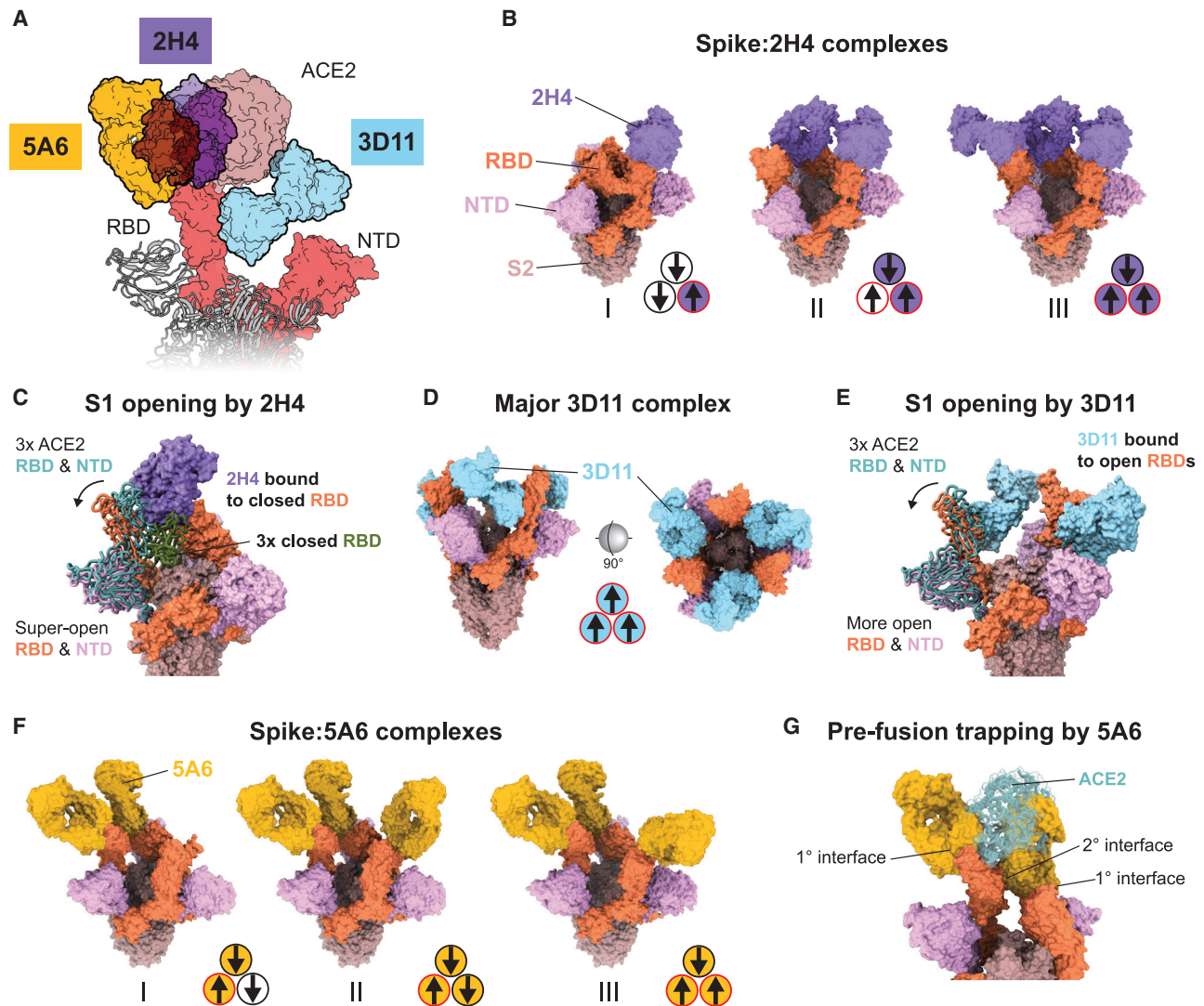


Figure 4. Structures of Spike-Fab complexes

(A) Schematic of three Fabs—5A6 (goldenrod), 2H4 (purple), and 3D11 (sky blue)—bound to the SARS-CoV-2 Spike protein. All Fabs are shown in relation to the complex formed by an open RBD (red) and the extracellular domain of ACE2 (rose brown).

(B) Spike:2H4 complexes depicted as surface models, with 2H4 in purple, RBDs in coral, NTDs in plum, and the S2 core in rose brown. Triads of small circles to the lower left of each complex figure represent the three RBDs, with an inset arrow indicating the open (up) or closed (down) conformation and purple fill indicating a bound Fab. The ensemble of Spike:2H4 complexes is reminiscent of several intermediates in the conformational cycle triggered by serial binding of ACE2.

(C) A cutaway of Spike:2H4 complex II, highlighting the steric effect of 2H4 bound to a closed RBD on the counterclockwise adjacent RBD and NTD. The 2H4-bound RBD clashes with both RBDs from the fully closed trimer conformation (PDB: 6ZGI; dark green) and the fully opened conformation with three ACE2 molecules (PDB: 7A98; cadet blue).

(D) The single major Spike:3D11 complex with colors as in (B) (3D11 in sky blue). All RBDs are open, resembling the open trimer bound to three copies of ACE2. Right: the extracellular view along the Spike trimer axis reveals its S2 core essentially unsheathed.

(E) A cutaway of the Spike:3D11 complex, showing that its effect on the neighboring RBD is similar to that of 2H4 but less pronounced. Colors are as in (C), with 3D11 in sky blue.

(F) Spike:5A6 complexes with colors as in (B) and 5A6 in goldenrod. Each complex exhibits the same quaternary state across two RBDs, with 5A6 bound between one closed RBD and a counterclockwise adjacent open RBD also bearing a copy of 5A6. The third RBD is usually open and may also bind 5A6.

(G) The quaternary epitope seen in all Spike:5A6 complexes involves two distinct interfaces and appears to trap the pre-fusion Spike by locking closed one RBD. Binding to either interface results in steric occlusion of ACE2 (PDB: 7A94; cadet blue) from the RBD. Both Fabs synergistically block ACE2 binding to the open RBD, whereas the Fab at the quaternary epitope blocks ACE2 binding to two RBDs simultaneously.

See also [Figures S3, S4, and S5](#); [Table S3](#); and [Videos S1, S2, and S3](#).

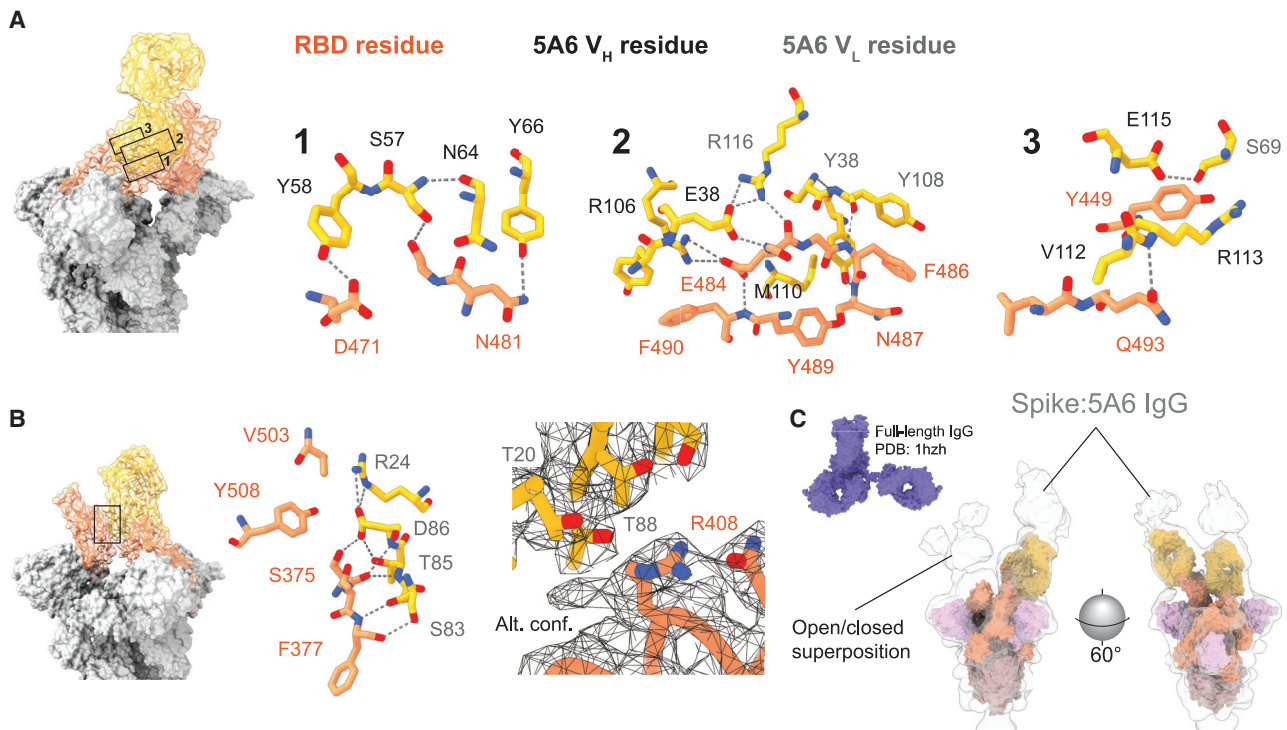


Figure 5. Binding mode and epitope of 5A6

(A) A tour of the primary interface between the Spike RBD and 5A6, using three immediately adjacent cross-sections along the viewing axis. Spike residues and labels are colored in coral or by heteroatom, and 5A6 residues are colored goldenrod, with labels for V_H residues in black and V_L residues in gray. Fab residue labels use the international ImMunoGeneTics information system (IMGT) (Lefranc et al., 2003). Predicted hydrogen bonds are shown as dashed gray lines. The interface features extensive hydrogen bonding, numerous hydrophobic contacts, and multiple salt bridges. A aromatic cluster formed by 5A6 V_L Y38 and Y108, and RBD F486; a salt bridge between 5A6 V_H R106 and RBD E484; and a cation- π interaction between Fab V_H R112 and RBD Y449 are particularly notable.

(B) The secondary interface between 5A6 and the neighboring open RBD comprises mostly hydrogen bonds, many of which involve main-chain atoms. Atom and label colors are as in (A). An interesting feature is stabilization of an alternate conformation of RBD R408 by 5A6 V_L T20 and T88.

(C) Two views of the Spike:5A6 IgG complex cryo-EM map (translucent gray) overlaid on the surface model of Spike:5A6 Fab complex I (colors as in Figure 4). The docked Fab complex model and the IgG complex cryo-EM density reveal a congruent epitope binding geometry in both formats, with two RBDs in the characteristic open/closed trapped conformation. Fc domains are visible as unmodeled blobs to the back of each Fab and are like a superposition of multiple possible stoichiometries. The third RBD seems to be a superposition of open and closed RBDs with IgG bound. The surface model of a full-length human IgG X-ray crystal structure (PDB: 1HZH) is shown for scale (comparison is facilitated by use of orthographic projection).

compared with the RBD (Figure S2D). 3D classification reveals outward motions of the NTD and variation in Fab occupancy, but only open RBDs are observed (Figure S4A). As for 2H4, the 3D11-bound RBDs are “more open” (displaced further outward) than those in the triple ACE2 complex (Figure 4E).

Although its epitope does not significantly overlap with the ACE2-RBD interface, 3D11 nevertheless effectively blocks ACE2 binding and stabilizes a quaternary state of the Spike, with three open RBDs and NTDs, that closely resembles the penultimate stage of ACE2-induced Spike opening (Benton et al., 2020). We therefore call 3D11 an allosteric receptor-mimetic antibody that does not directly target the ACE2 interface but prevents ACE2 binding and enhances Spike-mediated fusion by rapidly advancing the Spike conformational cycle to its final stages.

5A6 traps a pre-fusion conformation to inhibit Spike-mediated fusion

Multiple states of the Spike:5A6 complex were resolved to better than 3.0 Å, with local resolution sufficient for accurate modeling

of the Fab-RBD interface (Figure S3G). 5A6 recognizes surface loops near the tip of the RBD, which are solvent exposed even when all RBDs are closed. The binding geometry is permissive for any trimer configuration and any stoichiometry without steric constraints from Spike or Fab. Despite this complete conformational freedom, all 5A6 complexes feature at least two 5A6 Fabs bound to an open RBD counterclockwise adjacent in turn from a closed RBD (Figure 4F). The hallmark of these states is a cryptic quaternary epitope in which a region of the Fab V_L domain makes a second interaction with an adjacent open RBD (Figure 4G). This new interaction is not possible with a closed RBD and requires an adjustment away from the average positions of open RBDs in other structures (Figure S4B). The closed RBD bound via the main 5A6 interface is also displaced from other closed conformations.

CDR loops H1, H2, H3, and L1 engage the canonical epitope with a buried surface area of 850 Å² (Figure 5A). Partial overlap of the RBM and Fab interface and a clash induced between ACE2 and the Fab V_L domain, are likely sufficient to exclude

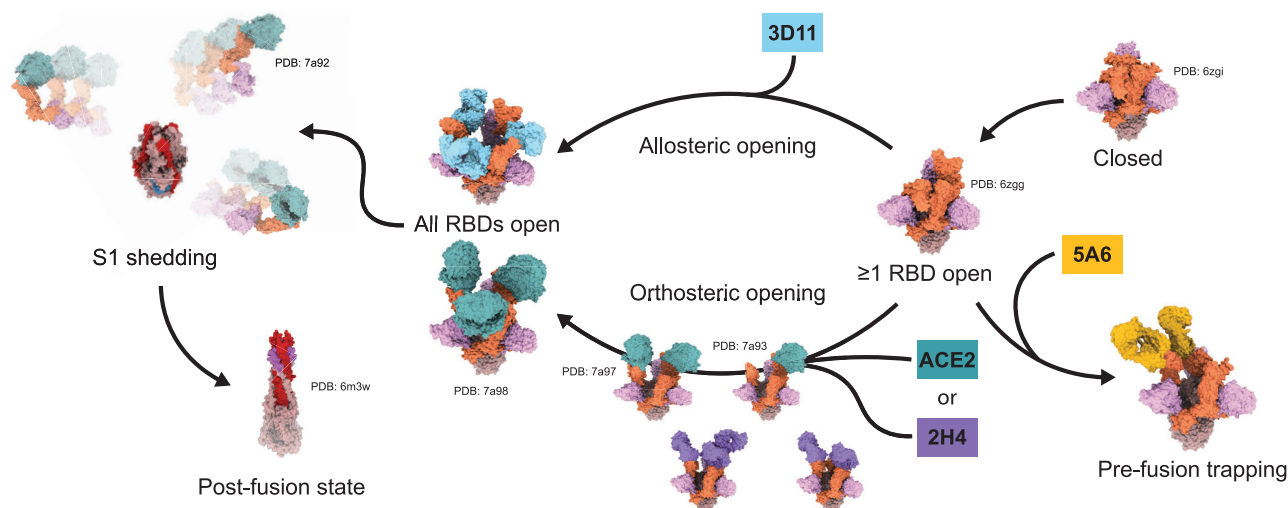


Figure 6. Spike functional modulation by receptor-blocking antibodies

A schematic model representing the possible effects of receptor-blocking antibodies, and ACE2 itself, on the conformational cycle of the SARS-CoV-2 Spike trimer. On the virus surface, the Spike is found predominantly in the closed conformation or a “receptor-seeking” conformation with one RBD open. When serially bound by ACE2 or an orthosteric mimetic antibody like 2H4, the Spike trimer passes through a series of conformations that eventually permit S1 shedding and the S2 post-fusion transition that mediates membrane fusion. Alternatively, allosteric antibodies such as 3D11 can advance the trimer directly to the end of the opening process, potentiating formation of syncytia through fusion of neighboring cells. Allosteric opening most likely contributes to lower potency in a high-affinity receptor-blocking antibody and might even suggest the possibility of antibody-dependent enhancement of infection. Finally, the Spike might instead be recognized by 5A6, which inhibits membrane fusion and syncytium formation by preventing S1 shedding and trapping the pre-fusion trimer. By enjoining the exposure and conformational transition of the S2 subunit, the 5A6 complex represents an unproductive dead end for the Spike trimer.

See also [Figure S6](#).

ACE2 from the RBD. The second interaction contributes an additional 363 \AA^2 (Figure 5B), and the C_{H1} and C_L domains of 5A6 at the cryptic quaternary epitope induce an even more severe clash with ACE2 (Figure 4G). Two Fabs thus act synergistically to block ACE2 binding, whereas one Fab is capable of blocking ACE2 at two RBDs simultaneously. The secondary interface must be released for the bound RBD to open, and we hypothesize that 5A6 at its quaternary epitope locks one RBD closed, arresting the trimer in its pre-fusion state. Precise conservation of the binding mode and the cryptic quaternary epitope from free Fab to IgG is confirmed by a structure of 5A6 IgG complexed with the Spike trimer at $\sim 15\text{-\AA}$ resolution (Figure 5C). Although the Fc domain is not well resolved because of the flexibility of the hinge region, the structures suggest that 5A6 IgG may bind to two RBDs from the same trimer (Figure S4C) and shows that no steric effects preclude binding of three IgGs at sufficient concentration. Noting the weak potentiation of syncytium formation by 5A6 Fab, we deduce that the cryptic epitope likely appears following initial Fab binding and leads to cooperative action against SARS-CoV-2 by imbuing a second binding event with enhanced affinity and receptor blockade. We also conclude that the geometry of the quaternary epitope and avidity of 5A6 IgG drive robust pre-fusion conformational trapping and potent inhibition of Spike-mediated fusion and syncytium formation.

DISCUSSION

Receptor engagement to a Spike RBD locks it in the open conformation and triggers a cooperative process in which the Spike

conformational ensemble is driven toward further opening by successive rounds of receptor binding (Benton et al., 2020). The process culminates in unshathing of the S2 subunit and, following proteolytic cleavage, shedding of the S1-ACE2 subcomplex. S1 shedding, in turn, facilitates the post-fusion state transition, leading to membrane fusion and virus entry. The Spike protein on the surface of infected cells can also mediate ACE2-dependent fusion of neighboring cells to form multinucleated giant cells, presumably through the same cycle of proteolysis and conformational transitions. Genetic variation in Spike, in and outside of the RBM, can influence function by altering the conformational equilibrium of the trimer, as seen for the D614G variant, which more readily populates states with multiple open RBDs (Yurkovetskiy et al., 2020) and exhibits heightened infectivity (Korber et al., 2020).

We identified six receptor-blocking antibodies that exhibit differences in avidity, binding mode, and neutralization of the live virus despite the fact that all of them have similarly high affinities for the RBD of the viral Spike protein. Strikingly, one highly potent neutralizing antibody inhibits Spike-mediated syncytium formation, whereas another, more weakly neutralizing antibody actually potentiates cell-cell fusion. These findings suggest that the potential effectiveness of a neutralizing antibody is influenced by a number of possibly countervailing factors, highlighting a complex basis for viral neutralization potency, *contra* a simplistic view where receptor blocking and affinity enhancement through avidity are the sole determinants of viral neutralization. Cryo-EM structures reveal the conformational landscapes of three Spike-Fab complexes and provide 3D mapping of antibody-Spike

epitopes, from which we can draw mechanistic insights that explain their distinct bioactivities in terms of the known intermediates in Spike opening (Figure 6). Certain receptor-blocking antibodies, such as 2H4, may function as orthosteric receptor mimetics conducive to the same cooperative processes as receptor binding. Another class of antibodies, exemplified by 3D11, act as allosteric effectors that advance the Spike directly to the final stages of S2 unseathing. In contrast, 5A6 possesses a unique binding mode that stabilizes a Spike conformation that prohibits S1 shedding and traps the pre-fusion state. We hypothesize that synergy between receptor blockade and pre-fusion trapping allows 5A6 to prevent targeted viral fusion and Spike-mediated cell-cell fusion.

Directly comparing the monovalent Fabs and bivalent IgGs also provides insight into the nature of avidity. The magnitude of binding and neutralization enhancement in the IgG format supports bivalent binding for all six antibodies (Vauquelin and Charlton, 2013). This result may be counterintuitive because modeling studies suggest that the hinge linking IgG Fc and Fab domains may have difficulty bridging the gaps seen in our structures of Spike:Fab complexes (Figure S4C). On the other hand, our structure of the 5A6 IgG complex confirms that 5A6 Fab and IgG forms do bind with congruent geometries, and a morph between 5A6 Fab bound to closed and open RBDs shows that shorter distances between Fabs do obtain for intermediate RBD conformations (Video S3). These results may imply that high-affinity bivalent binding to intermediate RBD conformations is replaced by high-density monovalent binding as the concentration of 5A6 IgG increases. In contrast to 5A6, 3D11 and 2H4 Spike:IgG complexes were not tractable for single-particle cryo-EM (Figure S4E). Qualitative image analysis suggests that these species do not trap defined conformational states of the Spike trimer, and that 3D11 in particular may achieve virus neutralization by destabilizing the Spike, as does the CR3022 antibody with a similar epitope (Huo et al., 2020). Intriguingly, we found that 3D11 has greatly reduced potency against the pseudovirus bearing D614G Spike, whereas that of 5A6 is slightly improved, although position 614 is outside of the RBD and far from the epitope of either antibody in the RBD (Figure S6). The D614G mutant Spike is known to occupy states with multiple open RBDs (Yurkovetskiy et al., 2020) and has been found to shed the S1 subunit less readily than the original SARS-CoV-2 Spike protein (Zhang et al., 2020). We can thus understand altered neutralization of D614G pseudovirus by 3D11 and 5A6 in terms of the model in Figure 6 because the effects of both antibodies are mediated by open RBD conformations that represent immediately available binding sites for 3D11 and present the full quaternary epitope of 5A6. The reduced S1 shedding of the more stable D614G Spike may also assist with the pre-fusion trapping activity of 5A6 while conveying resistance against trimer denaturation by 3D11.

The quaternary epitope recognized by 5A6 conveys cooperative binding as well as avidity, and both aspects may hinder virus escape via mutations in Spike protein (Barnes et al., 2020). In summary, our work establishes a platform for exploring allosteric control surfaces across the SARS-CoV-2 Spike protein. Although we employ syncytium formation as a general model for Spike protein function, pre-fusion trapping by 5A6 may convey greater efficacy against late-stage or severe illness because of the role of

syncytia in COVID-19 pathology (Bussani et al., 2020). Notably, cell-cell fusion during respiratory syncytial virus (RSV) infection also leads to severe tissue damage, and the therapeutic antibody palivizumab is known to trap a pre-fusion state of the fusogenic F protein of RSV (Huang et al., 2010). Uncovering the particular modes of action and functional consequences of Spike binders in general may deepen our understanding of avidity, virus neutralization, and disruption of syncytium formation and play a role in development of therapeutic agents or vaccines during the ongoing COVID-19 pandemic.

Limitations of study

Despite providing structural insights into Spike function in mediating cell-cell fusion, our study does not address how antibodies may influence specific biochemical events preceding fusion, such as proteolytic cleavage. Furthermore, a number of Spike sequences with mutations in addition to D614G have now been reported, and the specific interplay between Spike sequence variation and the conformational changes elicited by antibody binding still remains to be understood.

STAR★METHODS

Detailed methods are provided in the online version of this paper and include the following:

- KEY RESOURCES TABLE
- RESOURCE AVAILABILITY
 - Lead contact
 - Materials availability
 - Data and code availability
- EXPERIMENTAL MODEL AND SUBJECT DETAILS
 - Cells
 - HAE
 - Virus
- METHOD DETAILS
 - Antibody discovery from phage display library
 - IgG expression and purification
 - Fab production and purification
 - Avidity binding ELISA to RBD proteins
 - Avidity binding ELISA to purified pseudovirus
 - Competition ELISA
 - Conversion of IgG antibodies to Fab fragments
 - Soluble SARS-CoV-2 Spike production
 - Cryo-EM sample preparation and imaging
 - Image processing
 - Molecular modeling
 - Generation of pseudovirus particles
 - Purification of pseudovirus particles
 - Pseudovirus neutralization assay
 - Live virus neutralization assay in Vero E6 cells
 - Live virus neutralization assay in HAE
 - Cell-cell fusion assay
 - Fab affinity measurement by BLI
 - Avidity binding by BLI
 - Epitope binning by BLI
 - IgG and Fab affinity for Spike trimer by SPR
 - Statistical analysis

SUPPLEMENTAL INFORMATION

Supplemental information can be found online at <https://doi.org/10.1016/j.cell.2021.04.033>.

ACKNOWLEDGMENTS

We thank Prof. Yee-Joo Tan (Department of Microbiology, NUS; Institute of Molecular and Cell Biology, A*STAR) who kindly provided CHO-ACE2 cells. We also thank Wong Pui San and Chye De Ho in the BSL 3 facility (DSO National Laboratories) as well as Dr. Pei Yin Lim and Siti Nazihah Mohd Salleh (Singapore Immunology Network) for technical assistance. We thank Prof. Jason McLellan (University of Texas at Austin) for the prefusion S ectodomain and Prof. Joseph DeRisi, Prof. Robert Fletterick (UCSF), and Dr. John Pak (CZI Biohub, San Francisco) for helpful discussions. This work was supported by core research grants provided to the Singapore Immunology Network by the Biomedical Research Council (BMRC) and the ACCELERATE GAP fund (ACCL/19-GAP064-R20H-I) from the Agency of Science, Technology and Research (A*STAR, Singapore) (to C.-I.W.). S.M.-S. was supported by NMRC grant COVID19RF-004. Support was also provided by National Institutes of Health grants P50AI150476 (to C.S.C. and Y.C.), S10OD020054 (to Y.C.), and S10OD021741 (to Y.C.). This work was supported by the UCSF COVID-19 Response Fund, a grant from Allen & Company, and supporters of the UCSF Program for Breakthrough Biomedical Research (PBBR), which was established with support from the Sandler Foundation (to C.S.C., Y.C., and A.M.). Additional support was provided by a fast grant from Emergent Ventures at the Mercatus Center, George Mason University (to C.S.C.). Y.C. is an Investigator of the Howard Hughes Medical Institute. Additional support was provided by INSERM REACTing (Research & Action Emerging Infectious Diseases), CNRS, and Institut Mérieux (Mérieux research grant) (to A.P., O.T., and M.R.-C.).

AUTHOR CONTRIBUTIONS

B.W., D.A., W.-H.L., Y.H., C.-W.H., B.F., P.M.L.N., E.Z.X.N., M.B., D.B., S.M.-S., M.R.-C., A.M., Y.C., C.S.C., and C.-I.W. conceptualized and designed the study. L.R., B.J.H., M.R.-C., A.M., Y.C., C.S.C., and C.-I.W. coordinated the study. B.W., D.A., W.-H.L., Y.H., C.-W.H., B.F., P.M.L.N., E.Z.X.N., M.B., D.B., A.P., B.A., H.C.T., C.Y.L., R.A.M., A.P., O.T., M.K.S., F.J.T., Y.Y.C.Y., S.G.K.S., C.E.Z.C., E.C., and N.J.Y. conducted the experiments. B.W., D.A., W.-H.L., Y.H., C.-W.H., B.F., P.M.L.N., E.Z.X.N., M.B., D.B., H.C.T., C.Y.L., R.A.M., A.P., B.A., O.T., S.G.K.S., C.E.Z.C., S.M.-S., L.R., M.R.-C., A.M., Y.C., C.S.C., and C.-I.W. analyzed and interpreted the data. D.A., B.W., W.-H.L., Y.H., C.-W.H., B.F., P.M.L.N., E.Z.X.N., M.B., D.B., A.P., O.T., C.E.Z.C., S.M.-S., L.R., B.J.H., M.R.-C., A.M., Y.C., C.S.C., and C.-I.W. wrote and revised the manuscript. All authors read and approved the final manuscript.

DECLARATION OF INTERESTS

B.W., W.-H.L., C.-W.H., Y.H., P.M.L.N., E.Z.X.N., H.C.T., C.Y.L., R.A.M., M.K.S., F.J.T., Y.Y.C.Y., and C.-I.W. are listed as inventors of a filed patent for all 27 monoclonal antibodies mentioned in this manuscript.

Received: November 18, 2020

Revised: February 19, 2021

Accepted: April 19, 2021

Published: April 24, 2021

REFERENCES

Afonine, P.V., Poon, B.K., Read, R.J., Sobolev, O.V., Terwilliger, T.C., Urzhumtsev, A., and Adams, P.D. (2018). Real-space refinement in PHENIX for cryo-EM and crystallography. *Acta Crystallogr. D Struct. Biol.* **74**, 531–544.

Barnes, C.O., Jette, C.A., Abernathy, M.E., Dam, K.A., Esswein, S.R., Gristick, H.B., Malutin, A.G., Sharaf, N.G., Huey-Tubman, K.E., Lee, Y.E., et al. (2020).

SARS-CoV-2 neutralizing antibody structures inform therapeutic strategies. *Nature* **588**, 682–687.

Benton, D.J., Wrobel, A.G., Xu, P., Roustan, C., Martin, S.R., Rosenthal, P.B., Skehel, J.J., and Gamblin, S.J. (2020). Receptor binding and priming of the spike protein of SARS-CoV-2 for membrane fusion. *Nature* **588**, 327–330.

Brouwer, P.J.M., Caniels, T.G., van der Straten, K., Snitselaar, J.L., Aldon, Y., Bangaru, S., Torres, J.L., Okba, N.M.A., Claireaux, M., Kerster, G., et al. (2020). Potent neutralizing antibodies from COVID-19 patients define multiple targets of vulnerability. *Science* **369**, 643–650.

Burton, D.R., Saphire, E.O., and Parren, P.W. (2001). A model for neutralization of viruses based on antibody coating of the virion surface. *Curr. Top. Microbiol. Immunol.* **260**, 109–143.

Bussani, R., Schneider, E., Zentilin, L., Collesi, C., Ali, H., Braga, L., Volpe, M.C., Colliva, A., Zanconati, F., Berlot, G., et al. (2020). Persistence of viral RNA, pneumocyte syncytia and thrombosis are hallmarks of advanced COVID-19 pathology. *EBioMedicine* **61**, 103104.

Cao, Y., Su, B., Guo, X., Sun, W., Deng, Y., Bao, L., Zhu, Q., Zhang, X., Zheng, Y., Geng, C., et al. (2020). Potent Neutralizing Antibodies against SARS-CoV-2 Identified by High-Throughput Single-Cell Sequencing of Convalescent Patients' B Cells. *Cell* **182**, 73–84.e16.

Chi, X., Yan, R., Zhang, J., Zhang, G., Zhang, Y., Hao, M., Zhang, Z., Fan, P., Dong, Y., Yang, Y., et al. (2020). A neutralizing human antibody binds to the N-terminal domain of the Spike protein of SARS-CoV-2. *Science* **369**, 650–655.

Croll, T.I. (2018). ISOLDE: a physically realistic environment for model building into low-resolution electron-density maps. *Acta Crystallogr. D Struct. Biol.* **74**, 519–530.

Dowd, K.A., and Pierson, T.C. (2011). Antibody-mediated neutralization of flaviviruses: a reductionist view. *Virology* **411**, 306–315.

Flamand, A., Raux, H., Gaudin, Y., and Ruigrok, R.W.H. (1993). Mechanisms of rabies virus neutralization. *Virology* **194**, 302–313.

Frenzel, A., Kügler, J., Helmsing, S., Meier, D., Schirrmann, T., Hust, M., and Dübel, S. (2017). Designing Human Antibodies by Phage Display. *Transfus. Med. Hemother.* **44**, 312–318.

Goddard, T.D., Huang, C.C., Meng, E.C., Pettersen, E.F., Couch, G.S., Morris, J.H., and Ferrin, T.E. (2018). UCSF ChimeraX: Meeting modern challenges in visualization and analysis. *Protein Sci.* **27**, 14–25.

Goh, A.X., Bertin-Maghit, S., Ping Yeo, S., Ho, A.W., Derks, H., Mortellaro, A., and Wang, C.-I. (2014). A novel human anti-interleukin-1 β neutralizing monoclonal antibody showing in vivo efficacy. *MAbs* **6**, 765–773.

Hansen, J., Baum, A., Pascal, K.E., Russo, V., Giordano, S., Wloga, E., Fulton, B.O., Yan, Y., Koon, K., Patel, K., et al. (2020). Studies in humanized mice and convalescent humans yield a SARS-CoV-2 antibody cocktail. *Science* **369**, 1010–1014.

Hoffmann, M., Kleine-Weber, H., Schroeder, S., Krüger, N., Herrler, T., Erichsen, S., Schiergens, T.S., Herrler, G., Wu, N.-H., Nitsche, A., et al. (2020). SARS-CoV-2 Cell Entry Depends on ACE2 and TMPRSS2 and Is Blocked by a Clinically Proven Protease Inhibitor. *Cell* **181**, 271–280.e8.

Huang, K., Incognito, L., Cheng, X., Ulbrandt, N.D., and Wu, H. (2010). Respiratory syncytial virus-neutralizing monoclonal antibodies motavizumab and palivizumab inhibit fusion. *J. Virol.* **84**, 8132–8140.

Huo, J., Zhao, Y., Ren, J., Zhou, D., Duyvesteyn, H.M.E., Ginn, H.M., Carrique, L., Malinauskas, T., Ruza, R.R., Shah, P.N.M., et al. (2020). Neutralization of SARS-CoV-2 by Destruction of the Prefusion Spike. *Cell Host Microbe* **28**, 445–454.e6.

Ju, B., Zhang, Q., Ge, J., Wang, R., Sun, J., Ge, X., Yu, J., Shan, S., Zhou, B., Song, S., et al. (2020). Human neutralizing antibodies elicited by SARS-CoV-2 infection. *Nature* **584**, 115–119.

Koot, M., Keet, I.P.M., Vos, A.H.V., de Goede, R.E.Y., Roos, M.Th.L., Coutinho, R.A., Miedema, F., Schellekens, P.Th.A., and Tersmette, M. (1993). Prognostic value of HIV-1 syncytium-inducing phenotype for rate of CD4+ cell depletion and progression to AIDS. *Ann. Intern. Med.* **118**, 681–688.

- Korber, B., Fischer, W.M., Gnanakaran, S., Yoon, H., Theiler, J., Alfaller, W., Hengartner, N., Giorgi, E.E., Bhattacharya, T., Foley, B., et al.; Sheffield COVID-19 Genomics Group (2020). Tracking Changes in SARS-CoV-2 Spike: Evidence that D614G Increases Infectivity of the COVID-19 Virus. *Cell* **182**, 812–827.e19.
- Lan, J., Ge, J., Yu, J., Shan, S., Zhou, H., Fan, S., Zhang, Q., Shi, X., Wang, Q., Zhang, L., and Wang, X. (2020). Structure of the SARS-CoV-2 spike receptor-binding domain bound to the ACE2 receptor. *Nature* **581**, 215–220.
- Lefranc, M.-P., Pommié, C., Ruiz, M., Giudicelli, V., Foulquier, E., Truong, L., Thouvenin-Contet, V., and Lefranc, G. (2003). IMGT unique numbering for immunoglobulin and T cell receptor variable domains and Ig superfamily V-like domains. *Dev. Comp. Immunol.* **27**, 55–77.
- Lescure, F.-X., Bouadma, L., Nguyen, D., Parisey, M., Wicky, P.-H., Behillil, S., Gaymard, A., Bouscambert-Duchamp, M., Donati, F., Le Hingrat, Q., et al. (2020). Clinical and virological data of the first cases of COVID-19 in Europe: a case series. *Lancet Infect. Dis.* **20**, 697–706.
- Liu, H., Wu, N.C., Yuan, M., Bangaru, S., Torres, J.L., Caniels, T.G., van Schooten, J., Zhu, X., Lee, C.D., Brouwer, P.J.M., et al. (2020). Cross-Neutralization of a SARS-CoV-2 Antibody to a Functionally Conserved Site Is Mediated by Avidity. *Immunity* **53**, 1272–1280.e5.
- Lou, Y., Zhao, W., Wei, H., Chu, M., Chao, R., Yao, H., Su, J., Li, Y., Li, X., Cao, Y., et al. (2020). Cross-neutralization antibodies against SARS-CoV-2 and RBD mutations from convalescent patient antibody libraries. *bioRxiv*. <https://doi.org/10.1101/2020.06.06.137513>.
- Lu, R.-M., Hwang, Y.-C., Liu, I.-J., Lee, C.-C., Tsai, H.-Z., Li, H.-J., and Wu, H.-C. (2020). Development of therapeutic antibodies for the treatment of diseases. *J. Biomed. Sci.* **27**, 1.
- Mastrorade, D.N. (2005). Automated electron microscope tomography using robust prediction of specimen movements. *J. Struct. Biol.* **152**, 36–51.
- McNamara, P.S., and Smyth, R.L. (2002). The pathogenesis of respiratory syncytial virus disease in childhood. *Br. Med. Bull.* **61**, 13–28.
- Musarrat, F., Chouljenko, V., Dahal, A., Nabi, R., Chouljenko, T., Jois, S.D., and Kousoulas, K.G. (2020). The anti-HIV drug nelfinavir mesylate (Viracept) is a potent inhibitor of cell fusion caused by the SARSCoV-2 spike (S) glycoprotein warranting further evaluation as an antiviral against COVID-19 infections. *J. Med. Virol.* **92**, 2087–2095.
- Ng, O.-W., Keng, C.-T., Leung, C.S.-W., Peiris, J.S.M., Poon, L.L.M., and Tan, Y.-J. (2014). Substitution at aspartic acid 1128 in the SARS coronavirus spike glycoprotein mediates escape from a S2 domain-targeting neutralizing monoclonal antibody. *PLoS ONE* **9**, e102415.
- Pettersen, E.F., Goddard, T.D., Huang, C.C., Couch, G.S., Greenblatt, D.M., Meng, E.C., and Ferrin, T.E. (2004). UCSF Chimera—a visualization system for exploratory research and analysis. *J. Comput. Chem.* **25**, 1605–1612.
- Pinto, D., Park, Y.-J., Beltramello, M., Walls, A.C., Tortorici, M.A., Bianchi, S., Jaconi, S., Culap, K., Zatta, F., De Marco, A., et al. (2020). Cross-neutralization of SARS-CoV-2 by a human monoclonal SARS-CoV antibody. *Nature* **583**, 290–295.
- Pizzorno, A., Padey, B., Julien, T., Trouillet-Assant, S., Traversier, A., Errazuriz-Cerda, E., Fouret, J., Dubois, J., Gaymard, A., Lescure, F.-X., et al. (2020). Characterization and Treatment of SARS-CoV-2 in Nasal and Bronchial Human Airway Epithelia. *Cell Rep. Med.* **1**, 100059.
- Punjani, A., and Fleet, D.J. (2021). 3D variability analysis: Resolving continuous flexibility and discrete heterogeneity from single particle cryo-EM. *J. Struct. Biol.* **213**, 107702.
- Punjani, A., Rubinstein, J.L., Fleet, D.J., and Brubaker, M.A. (2017). cryo-SPARC: algorithms for rapid unsupervised cryo-EM structure determination. *Nat. Methods* **14**, 290–296.
- Rogers, T.F., Zhao, F., Huang, D., Beutler, N., Burns, A., He, W.T., Limbo, O., Smith, C., Song, G., Woehl, J., et al. (2020). Isolation of potent SARS-CoV-2 neutralizing antibodies and protection from disease in a small animal model. *Science* **369**, 956–963.
- Saphire, E.O., Schendel, S.L., Fusco, M.L., Gangavarapu, K., Gunn, B.M., Wec, A.Z., Halfmann, P.J., Brannan, J.M., Herbert, A.S., Qiu, X., et al.; Viral Hemorrhagic Fever Immunotherapeutic Consortium (2018). Systematic analysis of monoclonal antibodies against Ebola virus GP defines features that contribute to protection. *Cell* **174**, 938–952.e13.
- Scheres, S.H.W. (2012). A Bayesian view on cryo-EM structure determination. *J. Mol. Biol.* **415**, 406–418.
- Schneider, J., Pease, D., Navaratnarajah, C., Halfmann, P., Clemens, D., Ye, D., Kim, C., Barkhymer, A., Kohle, S., Banks, A., et al. (2020). SARS-CoV-2 direct cardiac damage through spike-mediated cardiomyocyte fusion. *Research Square*. <https://www.researchsquare.com/article/rs-95587/v1>.
- Shi, R., Shan, C., Duan, X., Chen, Z., Liu, P., Song, J., Song, T., Bi, X., Han, C., Wu, L., et al. (2020). A human neutralizing antibody targets the receptor-binding site of SARS-CoV-2. *Nature* **584**, 120–124.
- Shulla, A., Heald-Sargent, T., Subramanya, G., Zhao, J., Perlman, S., and Gallagher, T. (2011). A transmembrane serine protease is linked to the severe acute respiratory syndrome coronavirus receptor and activates virus entry. *J. Virol.* **85**, 873–882.
- Stanfield, R.L., Zemla, A., Wilson, I.A., and Rupp, B. (2006). Antibody elbow angles are influenced by their light chain class. *J. Mol. Biol.* **357**, 1566–1574.
- Sylwester, A., Murphy, S., Shutt, D., and Soll, D.R. (1997). HIV-induced T cell syncytia are self-perpetuating and the primary cause of T cell death in culture. *J. Immunol.* **158**, 3996–4007.
- Tai, W., He, L., Zhang, X., Pu, J., Voronin, D., Jiang, S., Zhou, Y., and Du, L. (2020). Characterization of the receptor-binding domain (RBD) of 2019 novel coronavirus: implication for development of RBD protein as a viral attachment inhibitor and vaccine. *Cell. Mol. Immunol.* **17**, 613–620.
- Tortorici, M.A., and Veesler, D. (2019). Structural insights into coronavirus entry. In *Advances in Virus Research*, F.A. Rey, ed. (Academic Press), pp. 93–116.
- Vaughan, T.J., Osbourn, J.K., and Tempest, P.R. (1998). Human antibodies by design. *Nat. Biotechnol.* **16**, 535–539.
- Vauquelin, G., and Charlton, S.J. (2013). Exploring avidity: understanding the potential gains in functional affinity and target residence time of bivalent and heterobivalent ligands. *Br. J. Pharmacol.* **168**, 1771–1785.
- Walls, A.C., Xiong, X., Park, Y.-J., Tortorici, M.A., Snijder, J., Quispe, J., Cameron, E., Gopal, R., Dai, M., Lanzavecchia, A., et al. (2019). Unexpected Receptor Functional Mimicry Elucidates Activation of Coronavirus Fusion. *Cell* **176**, 1026–1039.e15.
- Walls, A.C., Park, Y.-J., Tortorici, M.A., Wall, A., McGuire, A.T., and Veesler, D. (2020). Structure, Function, and Antigenicity of the SARS-CoV-2 Spike Glycoprotein. *Cell* **181**, 281–292.e6.
- Wan, J., Xing, S., Ding, L., Wang, Y., Gu, C., Wu, Y., Rong, B., Li, C., Wang, S., Chen, K., et al. (2020). Human-IgG-Neutralizing Monoclonal Antibodies Block the SARS-CoV-2 Infection. *Cell Rep.* **32**, 107918.
- Wang, C., Li, W., Drabek, D., Okba, N.M.A., van Haperen, R., Osterhaus, A.D.M.E., van Kuppeveld, F.J.M., Haagmans, B.L., Grosveld, F., and Bosch, B.-J. (2020). A human monoclonal antibody blocking SARS-CoV-2 infection. *Nat. Commun.* **11**, 2251.
- Webb, B., and Sali, A. (2016). Comparative Protein Structure Modeling Using MODELLER. *Curr. Protoc. Bioinformatics* **54**, 5.6.1–5.6.37.
- Wilson, I.A., and Stanfield, R.L. (1994). Antibody-antigen interactions: new structures and new conformational changes. *Curr. Opin. Struct. Biol.* **4**, 857–867.
- Wrapp, D., De Vlieger, D., Corbett, K.S., Torres, G.M., Wang, N., Van Breedam, W., Roose, K., van Schie, L., Hoffmann, M., Pöhlmann, S., et al.; VIB-CMB COVID-19 Response Team (2020a). Structural Basis for Potent Neutralization of Betacoronaviruses by Single-Domain Camelid Antibodies. *Cell* **181**, 1004–1015.e15.
- Wrapp, D., Wang, N., Corbett, K.S., Goldsmith, J.A., Hsieh, C.-L., Abiona, O., Graham, B.S., and McLellan, J.S. (2020b). Cryo-EM structure of the 2019-nCoV spike in the prefusion conformation. *Science* **367**, 1260–1263.
- Wu, Y., Wang, F., Shen, C., Peng, W., Li, D., Zhao, C., Li, Z., Li, S., Bi, Y., Yang, Y., et al. (2020). A noncompeting pair of human neutralizing antibodies block COVID-19 virus binding to its receptor ACE2. *Science* **368**, 1274–1278.

- Xu, Z., Shi, L., Wang, Y., Zhang, J., Huang, L., Zhang, C., Liu, S., Zhao, P., Liu, H., Zhu, L., et al. (2020). Pathological findings of COVID-19 associated with acute respiratory distress syndrome. *Lancet Respir. Med.* **8**, 420–422.
- Young, B.E., Ong, S.W.X., Kalimuddin, S., Low, J.G., Tan, S.Y., Loh, J., Ng, O.-T., Marimuthu, K., Ang, L.W., Mak, T.M., et al.; Singapore 2019 Novel Coronavirus Outbreak Research Team (2020). Epidemiologic Features and Clinical Course of Patients Infected With SARS-CoV-2 in Singapore. *JAMA* **323**, 1488–1494.
- Yuan, M., Wu, N.C., Zhu, X., Lee, C.D., So, R.T.Y., Lv, H., Mok, C.K.P., and Wilson, I.A. (2020). A highly conserved cryptic epitope in the receptor binding domains of SARS-CoV-2 and SARS-CoV. *Science* **368**, 630–633.
- Yurkovetskiy, L., Wang, X., Pascal, K.E., Tomkins-Tinch, C., Nyalile, T.P., Wang, Y., Baum, A., Diehl, W.E., Dauphin, A., Carbone, C., et al. (2020). Structural and Functional Analysis of the D614G SARS-CoV-2 Spike Protein Variant. *Cell* **183**, 739–751.e8.
- Zhang, L., Jackson, C.B., Mou, H., Ojha, A., Peng, H., Quinlan, B.D., Rangarajan, E.S., Pan, A., Vanderheiden, A., Suthar, M.S., et al. (2020). SARS-CoV-2 spike-protein D614G mutation increases virion spike density and infectivity. *Nat. Commun.* **11**, 6013.
- Zheng, S.Q., Palovcak, E., Armache, J.-P., Verba, K.A., Cheng, Y., and Agard, D.A. (2017). MotionCor2: anisotropic correction of beam-induced motion for improved cryo-electron microscopy. *Nat. Methods* **14**, 331–332.
- Zhou, G., and Zhao, Q. (2020). Perspectives on therapeutic neutralizing antibodies against the Novel Coronavirus SARS-CoV-2. *Int. J. Biol. Sci.* **16**, 1718–1723.
- Zhou, P., Yang, X.-L., Wang, X.-G., Hu, B., Zhang, L., Zhang, W., Si, H.-R., Zhu, Y., Li, B., Huang, C.-L., et al. (2020). A pneumonia outbreak associated with a new coronavirus of probable bat origin. *Nature* **579**, 270–273.

STAR★METHODS

KEY RESOURCES TABLE

REAGENT or RESOURCE	SOURCE	IDENTIFIER
Antibodies		
1A5	Laboratory of Cheng-I Wang	N/A
1A8	Laboratory of Cheng-I Wang	N/A
1B2	Laboratory of Cheng-I Wang	N/A
1B11	Laboratory of Cheng-I Wang	N/A
1C2	Laboratory of Cheng-I Wang	N/A
1C3	Laboratory of Cheng-I Wang	N/A
1D12	Laboratory of Cheng-I Wang	N/A
1E5	Laboratory of Cheng-I Wang	N/A
1F4	Laboratory of Cheng-I Wang	N/A
1H7	Laboratory of Cheng-I Wang	N/A
2C9	Laboratory of Cheng-I Wang	N/A
2C10	Laboratory of Cheng-I Wang	N/A
2C12	Laboratory of Cheng-I Wang	N/A
2D3	Laboratory of Cheng-I Wang	N/A
2G7	Laboratory of Cheng-I Wang	N/A
2H4	Laboratory of Cheng-I Wang	N/A
3A11	Laboratory of Cheng-I Wang	N/A
3C5	Laboratory of Cheng-I Wang	N/A
3D2	Laboratory of Cheng-I Wang	N/A
3D11	Laboratory of Cheng-I Wang	N/A
3E9	Laboratory of Cheng-I Wang	N/A
3F1	Laboratory of Cheng-I Wang	N/A
3F11	Laboratory of Cheng-I Wang	N/A
3H7	Laboratory of Cheng-I Wang	N/A
3H11	Laboratory of Cheng-I Wang	N/A
5A6	Laboratory of Cheng-I Wang	N/A
6F8	Laboratory of Cheng-I Wang	N/A
HRP conjugated anti-human Fc antibody	JACKSON ImmunoResearch	Cat#109-036-098; RRID: AB_2337596
HRP conjugated anti-human Fab antibody	JACKSON ImmunoResearch	Cat#109-036-097; RRID: AB_2337595
Bacterial and virus strains		
SARS-CoV-2 (isolated from a patient in Singapore)	Laboratory of Brendon John Hanson	N/A
SARS-CoV-2 BetaCoV/France/IDF0571/2020	Laboratory of Dr. Manuel Rosa-Calatrava; Pizzorno et al., 2020	EPI_ISL_411218
Chemicals, peptides, and recombinant proteins		
SARS-CoV-2 Spike protein RBD-mFc	Sino Biological	Cat#40592-V05H
human ACE2-Fc	This paper	N/A
OptiPrep (60% [wt/vol] iodixanol)	STEMCELL Technologies	Cat#07820
Lipofectamine 2000 Transfection Reagent	Invitrogen	Cat#11668-019
Dulbecco's modified Eagle's medium	Hyclone	Cat#SH30022.01
Fetal Bovine Serum (FBS)	GIBCO	Cat#10270-106
Penicillin-Streptomycin	GIBCO	Cat#15140-122
MEM Non-Essential Amino Acids Solution	GIBCO	Cat#11140-050
Geneticin Selective Antibiotic (G418 Sulfate)	GIBCO	Cat#10131-027

(Continued on next page)

Continued

REAGENT or RESOURCE	SOURCE	IDENTIFIER
Critical commercial assays		
Lenti-X p24 rapid titer kit	Takara Bio	Cat#632500
Luciferase Assay System	Promega	Cat#E1510
Viral ToxGlo Assay	Promega	Cat#G8941
TMB Substrate	Surmodics, BioFX	Cat#TMBW-1000-01
Experimental models: Cell lines		
ExpiCHO-S	Thermo Fisher Scientific	Cat#A29127
293T	ATCC	Cat#CRL-3216
Vero E6 C1008	ATCC	Cat#CRL-1586
CHO-ACE2	Laboratory of Yee-Joo Tan	N/A
MucilAir Nasal HAE	Epithelix SARL	Ref: EP02MP
MucilAir Bronchial HAE	Epithelix SARL	Ref: EP01MD
Oligonucleotides		
Forward primer HKU-ORF1b-nsp14F: 50-TGGGGYTTTACRGGTAACCT-30	Eurogentec	N/A
Reverse primer HKU-ORF1b-nsp14R: 50-AACRCGCTTAACAAGCACTC-30	Eurogentec	N/A
Probe HKU-ORF1b-nsp141P: 50- FAMTAGTTGTGATGCWATCATGACTAG- TAMRA-30	Eurogentec	N/A
SDM primer FL1-R682AR683A-F: CCA AACAAACTCACCCgcGgcGGCTAGGTC TGTTGCCAGC	Integrated DNA Technologies	N/A
SDM primer FL1-D614G-F: AAG TAGCCGCTTGTACCAAGgCG TCAATTGTACCGAGGTGCC	Integrated DNA Technologies	N/A
Recombinant DNA		
Plasmid: pMDLg/pRRE	Laboratory of Didier Trono	Addgene ID: 12251
Plasmid: pRSV-Rev	Laboratory of Didier Trono	Addgene ID: 12253
Plasmid: pHIV-luc-ZsGreen	Laboratory of Bryan Welm	Addgene ID: 39196
Plasmid: pTT5LnX-CoV-SP (codon optimized S gene of SARS-CoV-2, GenBank: YP_009724390.1)	Laboratory of Brendon John Hanson	N/A
Plasmid: pTT5LnX-CoV-SP-D614G	This paper	N/A
Software and algorithms		
GraphPad Prism version 7.03	GraphPad	https://www.graphpad.com/scientific-software/prism/
Quest Graph IC ₅₀ calculator AAT	AAT Bioquest	https://www.aatbio.com/tools/ic50-calculator
Octet System Data Acquisition Software version 9.0.0.4.	ForteBio	N/A
Biacore T200 Evaluation Software	Cytiva Life Sciences	N/A
cryoSPARC v2.7-3.1	Structura Biotechnology	https://cryosparc.com/
Relion 3.1	Laboratory of Molecular Biology, Medical Research Council	https://github.com/3dem/relion
UCSF ChimeraX 1.1	UCSF	https://www.cgl.ucsf.edu/chimerax/
ISOLDE 1.1.0	Cambridge Institute for Medical Research	https://isolde.cimr.cam.ac.uk/
Coot 0.9.4.1	Laboratory of Molecular Biology, Medical Research Council	https://www2.mrc-lmb.cam.ac.uk/personal/pemsley/coot/
Rosetta 3.12	RosettaCommons	https://www.rosettacommons.org/

RESOURCE AVAILABILITY

Lead contact

Further information and requests for resources and reagents should be directed to and will be fulfilled by the Lead Contact, Dr. Cheng-I Wang (Wang_Chengl@immunol.a-star.edu.sg).

Materials availability

All requests for resources and reagents should be directed to and will be fulfilled by the Lead Contact. All antibodies are proprietary and can be obtained through a Materials Transfer Agreement. Other materials will also be available from the Lead Contact with a completed Materials Transfer Agreement.

Data and code availability

Atomic coordinates and cryo-EM maps are deposited in EMDB and PDB as follows. Spike:5A6 complex I has accession codes PDB: 7KQB and EMD-22993. The focused refinement of Spike:5A6 using a mask including 5A6 and two RBDs has accession codes PDB: 7M71 and EMD-23707. Maps for Spike:5A6 complex II and III are provided as additional maps in the same entry. Spike:3D11 has accession codes PDB: 7KQE and EMD-22997. The focused refinement of Spike:3D11 using a mask including 3D11 and one RBD has accession codes PDB: 7M7B and EMD-23709. Cryo-EM maps only were deposited for Spike protein alone, with accession EMD-22995, as well as for Spike:2H4 complexes I-III, accession codes EMD-22994. Additional Supplemental Items are available from Mendeley Data at <https://doi.org/10.17632/2jsns6kdw.1>.

EXPERIMENTAL MODEL AND SUBJECT DETAILS

Cells

The human embryonic kidney epithelial cell 293T (ATCC, Cat#CRL-3216) and Vero E6 C1008 cells (ATCC, Cat#CRL-1586) were cultured in Dulbecco's modified Eagle's medium (Hyclone, Cat#SH30022.01) supplemented with 10% heat-inactivated FBS (GIBCO, Cat#10270-106) and 100 U/ml Penicillin-Streptomycin (GIBCO, Cat#15140-122). A stable cell line expressing human ACE2, CHO-ACE2 (a kind gift from Professor Yee-Joo Tan, IMCB, A*Star) ([Ng et al., 2014](#)) was maintained in Dulbecco's modified Eagle's medium supplemented with 10% heat-inactivated FBS, 1% MEM Non-Essential Amino Acids Solution (GIBCO, Cat#11140-050) and 0.5 mg/ml of GeneticinTM Selective Antibiotic (GIBCO, Cat#10131-027). All cells were maintained at 37°C and 5% CO₂ and were passaged by dissociating the cells with StemProTM AccutaseTM Cell Dissociation Reagent (GIBCO, Cat#A1110501) every 2 to 3 days.

HAE

MucilAirTM HAE (human airway epithelia) reconstituted from human primary cells obtained from nasal or bronchial biopsies were provided by Epithelix SARL (Geneva, Switzerland) and maintained in air-liquid interphase with specific culture medium in Costar Transwell inserts (Corning, NY, USA) according to the manufacturer's instructions.

Virus

The Singapore strain of SARS-CoV-2 live virus used in this study was isolated from a nasopharyngeal swab of a patient in Singapore ([Young et al., 2020](#)). The French strain of SARS-CoV-2 live virus used in this study was isolated from one of the first COVID-19 cases confirmed in France: a 47-year old female patient hospitalized in January 2020 in the Department of Infectious and Tropical Diseases, Bichat Claude Bernard Hospital, Paris ([Lescure et al., 2020](#)). The complete viral genome sequence was obtained using Illumina MiSeq sequencing technology, was then deposited after assembly on the GISAID EpiCoV platform (Accession ID EPI_ISL_411218) under the name BetaCoV/France/IDF0571/2020.

METHOD DETAILS

Antibody discovery from phage display library

Anti-SARS-CoV-2 Spike RBD antibodies were isolated from an HX02 human Fab phage display library (Humanyx Pte Ltd) via *in vitro* selection. Briefly, biopanning was performed using SARS-CoV-2 RBD (YP_009724390.1) (Arg319-Phe541) with a mouse Fc tag (Sino Biological, Cat#40592-V05H) biotinylated using the EZ-Link NHS-PEG4-Biotin labeling kit (Thermo Fisher Scientific, Cat#A39259). In both rounds of biopanning, biotinylated SARS-CoV-2 RBD-mFc protein (Sino Biological, Cat#40592-V05H) was immobilized on M280 streptavidin-coated magnetic beads (Life Technologies, Cat#11205D); 3.5×10^{12} cfu phage in 1ml 1% casein-PBS blocking buffer was used in the first round, and 1.64×10^{11} cfu phage were used in the second round. During the biopanning process, binders to mouse Fc were removed by pre-incubation of phage with 2 μ M mouse IgG before mixing with the RBD-mFc antigen. After two rounds of biopanning, the Fabs of selected clones were expressed in *E. coli* HB2151 cells (Stratagene) to screen for RBD binders by ELISA. Unique clones were identified by DNA sequencing.

IgG expression and purification

Fabs were reformatted into human IgG in the pTT5 vector (National Research Council of Canada) and the IgG antibodies were expressed using ExpiCHO expression system (Thermo Fisher Scientific) by transient co-transfection of plasmids expressing the heavy and light chain of each antibody clone. Eight days after transfection, ExpiCHO-S cell suspension was centrifuged for 10 min at 2000 rpm and filtered with 0.22 μm filter to remove the cells and debris. Antibodies were then purified from the culture supernatant using Protein G Agarose (Merck Millipore, Cat#16-266) following the manufacturer's instructions. After elution, the purified antibodies were dialyzed at 4°C for 4-20 hours against 1x PBS, for 3 times and concentrated to 1-2 mg/ml using 10MWCO Vivaspin 20 (Sartorius, Cat#VS2001).

Fab production and purification

The tag-less Fab fragments were produced using the ExpiCHO transient expression system. Eight days after transfection, ExpiCHO-S cell suspension was centrifuged and filtered; and Fab was purified from the filtered culture supernatant using cation exchange chromatography (CIEX) on AKTA FPLC System (GE Healthcare). In brief, the supernatant was concentrated to 2 mL using 10MWCO Viva-spin 20 (Sartorius), diluted 1:20 in Buffer A (20 mM Sodium Acetate, pH 5.2), filtered through 0.22 μm filter, and loaded onto Mono-S 5/50 GL column at a flow rate of 1 ml/min. Fab fragments were eluted in Buffer B (20 mM Sodium Acetate, pH 5.2 with 1 M Sodium Chloride) with a sequential linear gradient of 0% to 5% in 5 min, 5% to 15% in 30 min, and 15% to 100% in 20 min of Buffer B injection at a flow rate of 1 ml/min. The resulting purified Fab fragments were dialyzed at 4°C for 4-20 hours against 4 l of 20 mM Histidine, 150 mM NaCl, pH 6.6, for 3 times and concentrated to 1-2 mg/ml using 10MWCO Vivaspin 6 (Sartorius, Cat#VS0601).

Avidity binding ELISA to RBD proteins

Anti-SARS-CoV-2 Spike RBD IgG antibodies were tested in an ELISA against biotinylated recombinant SARS-CoV-2 Spike protein RBD-mFc (Sino Biological, Cat#40592-V05H) to assess binding avidity for the target. In brief, NeutrAvidin protein (Thermo Fisher Scientific, Cat#31000) was coated at 5 $\mu\text{g/ml}$ onto 96-well ELISA plates in coating buffer (8.4 g/L NaHCO_3 , 3.56 g/L Na_2CO_3 , pH 9.5) overnight at 4°C. After blocking with 1% Casein (Thermo Fisher Scientific, Cat#A37528) for two hours, biotinylated antigen at 0.2 $\mu\text{g/ml}$ was added to the plates and captured by NeutrAvidin during one-hour incubation at room temperature. After washing with 0.05% PBST for 5 times, the IgG antibodies were added at different concentrations with 3-fold dilutions in triplicate and incubated for one hour. The wells were then washed again with 0.05% PBST, followed by addition of HRP conjugated anti-human Fc antibody (1:3000, JACKSON ImmunoResearch, Cat#109-036-098). Finally, the wells were washed and the HRP activity was measured at 450 nm with addition of 3,3',5,5'-tetramethylbenzidine (TMB) substrate (Surmodics, BioFX®, Cat#TMBW-1000-01).

Avidity binding ELISA to purified pseudovirus

Anti-SARS-CoV-2 Spike RBD IgG or Fab antibodies were tested in an ELISA against iodixanol-gradient-purified SARS-CoV-2 pseudoviruses with an isotype IgG used as a negative control antibody. In brief, 1 $\mu\text{g/ml}$ of pseudoviral particles were coated in coating buffer onto 96-well ELISA plates overnight at 4°C. After blocking with 1% Casein (Thermo Fisher Scientific, #A37528) for two hours, serially diluted IgG or Fab antibodies starting from 20 nM (IgG) or 300 nM (Fab) with five-fold dilutions were added to the plates and incubated for an hour at room temperature. The wells were then washed again with 0.05% PBST, followed by addition of HRP conjugated anti-human Fc antibody (JACKSON ImmunoResearch, Cat#109-036-098) or HRP conjugated anti-human Fab antibody (JACKSON ImmunoResearch, Cat#109-036-097) for one-hour incubation before HRP activity was measured at 450 nm with addition of TMB substrate (Surmodics, BioFX®, Cat#TMBW-1000-01).

Competition ELISA

Anti-SARS-CoV-2 Spike RBD IgG antibodies were tested in a competition ELISA to assess their ability to block the Spike protein RBD from binding to human ACE2 protein. In brief, the recombinant human ACE2 protein with a human Fc tag (ACE2-Fc) was coated onto the 96-well ELISA plates in coating buffer overnight at 4°C and blocked with 1% Casein. Then different concentrations of anti-SARS-CoV-2 Spike RBD IgG antibodies were pre-incubated with 0.5 nM biotinylated Spike protein RBD-mFc (Sino Biological, Cat#40592-V05H) for one hour at room temperature before they were added to the ELISA plates coated with ACE2-Fc. After one-hour incubation, the wells were washed with 0.05% PBST for five times and HRP conjugated streptavidin (Biolegend, Cat#405210) was added at a dilution of 1:3000, and incubated for another one hour before HRP activity was measured at 450 nm with addition of TMB substrate (Surmodics, BioFX®, Cat#TMBW-1000-01).

Conversion of IgG antibodies to Fab fragments

Digestion reaction for each IgG was prepared using immobilized FabALACTICA microspin columns (Genovis). 100 μL of IgG at 5 mg/mL concentration in digestion buffer (150 mM sodium phosphate, pH 7.0) were incubated overnight on each column. Digested sample was further purified using a HiTrap Protein L column followed by size-exclusion chromatography (Superdex 75 10/300 GL) using an Äkta Pure FPLC (GE Healthcare).

Soluble SARS-CoV-2 Spike production

The expression plasmid containing the prefusion S ectodomain as used in [Wrapp et al. \(2020b\)](#) was kindly provided by Prof. Jason McLellan (University of Texas at Austin). This construct was used to transiently transfect high-density Chinese Hamster Ovary

(ExpiCHO) cells with ExpiFectamine per the “Max Titer” protocol provided (Thermo Fisher). Six days post-transfection, 0.2 μm -filtered supernatant was collected and incubated with Ni-Sepharose Excel (Cytiva Life Sciences) for batch purification. Eluate was collected, concentrated in a 50 MWCO Amicon Ultra-15 centrifugal filter unit (MilliporeSigma), and injected onto a Superose6 10/300 GL column equilibrated in 10 mM HEPES, 200 mM NaCl, pH 8.0 to isolate trimeric, monodisperse material for Fab/IgG complexing.

Cryo-EM sample preparation and imaging

2.5 μL of Spike-Fab complex at a concentration of 0.4 mg/mL was applied to a 300 mesh gold Quantifoil 1.2/1.3 holey carbon grid that was glow discharged for 30 s at 15 mA immediately before sample application. Grids were blotted using Whatman #1 filter paper for 8 or 10 s at a blot force of 0 at 4°C and 100% humidity using a Mark IV Vitrobot (Thermo Fisher) and plunge frozen into liquid ethane. Samples were loaded onto a Titan Krios transmission electron microscope (Thermo Fisher) equipped with a Gatan K3 direct electron detector (Gatan) and a Quantum GIF energy filter (Gatan) operated with a 20 eV slit width during image acquisition. The K3 camera was operated in CDS mode using super resolution. A nominal magnification of 105,000x was used, for a pixel size of 0.835 Å (0.4175 Å super resolution pixel size) at the sample. A dose rate of 8 $\text{e}^-/(\text{pix} \cdot \text{sec})$, or 11.5 $\text{e}^-/(\text{Å}^2 \cdot \text{sec})$, and a frame rate of 0.05 s/frame was used with a total exposure time of 5.9 s, for a total dose of 67.7 $\text{e}^-/\text{Å}^2$. Automated data collection was performed using SerialEM (Mastronarde, 2005).

Image processing

Dose-weighted, motion-corrected sums down-sampled to the physical pixel size were obtained from the super-resolution DED movies using UCSF Motioncor2 (Zheng et al., 2017). For the Spike trimer, CTF estimation was performed in cryoSPARC (Punjani et al., 2017) followed by blob-based particle picking, 2D classification, *ab initio* modeling, 3D classification, and 3D refinement. For images of antibody complexes, particles were instead picked using templates generated from the apo trimer structure, and the apo trimer was likewise used as an initial model in 3D classification. The resolution of the interface between the Spike RBD and the 5A6 Fab was further improved using naive focused refinements. Additional 3D classification of the Spike:3D11 complex was performed in Relion 3.1 (Scheres, 2012). Processing details are given in Table S3 and Figure S5.

Molecular modeling

For each Spike:Fab complex, a previously determined structure of the SARS-CoV-2 Spike protein, along with a full-length Fab homology model computed by MODELER (Webb and Sali, 2016), were simultaneously docked into cryo-EM density using UCSF Chimera (Pettersen et al., 2004). Spike with one open RBD and one copy of ACE2 bound (PDB: 7a94) was used with 5A6, Spike with three open RBDs and three copies of ACE2 bound (PDB: 7a98) was used with 3D11, and Spike with two open RBDs and one copy of ACE2 bound (PDB: 7a95) was used with 2H4. Missing segments and side chains in the RBDs were built using Coot. Interactive, density-restrained molecular dynamics simulations in ChimeraX (Goddard et al., 2018) and ISOLDE (Croll, 2018) were used to finalize the models, and atomic b-factors were calculated using PHENIX (Afonine et al., 2018). Models for the Spike:5A6 and Spike:3D11 complexes were first built into density maps from whole-particle cryo-EM reconstructions, and then further refined using maps from focused refinements of the Fab and Spike RBD. Maps of Spike:2H4 complexes were of lower resolution and model building was terminated after the docking step described above. Model statistics and density fit information are presented in Table S3 and Figure S5.

Generation of pseudovirus particles

Pseudotyped viral particles expressing SARS-CoV-2 Spike protein were produced by transfecting of 30 million 293T cells with 12 μg pMDLg/pRRE (a gift from Didier Trono, Addgene #12251), 6 μg pRSV-Rev (a gift from Didier Trono, Addgene #12253), 24 μg pHIV-Luc-ZsGreen (a gift from Bryan Welm, Addgene #39196) and 12 μg pTT5LnX-CoV-SP (expressing SARS-CoV-2 Spike protein, GenBank: YP_009724390.1, a kind gift from DSO National Laboratories) using Lipofectamine 2000 transfection reagent (Invitrogen, Cat#11668-019). The transfected cells were cultured at 37°C incubator for 3 days. Viral supernatant was harvested, centrifuged at 700 g for 10min to remove cell debris and filtered through a 0.45 μm filter unit (Sartorius, Cat#16555). Lenti-X p24 rapid titer kit (Takara Bio, Cat#632200) was used to quantify the viral titers following the manufacturer instructions. pTT5LnX-CoV-SP plasmid with D614G mutation was generated using QuickChange Lightning Multi Site-Directed Mutagenesis Kit (Agilent, Cat#210513) and was used to generate mutant pseudovirus expressing SARS-CoV-2 Spike protein carrying D614G mutation.

Purification of pseudovirus particles

To concentrate and purify the pseudovirus particles expressing the SARS-CoV-2 Spike glycoproteins, pre-cleared 40 mL viral supernatant was concentrated by 20% sucrose gradient centrifugation at 10,000 g for 4 hours at 4°C in an SW41 Ti rotor with no brake. Upon removal of supernatant, 1 mL of PBS was added to the virus pellet and left at 4°C overnight. Concentrated virus was further purified by an OptiPrep (60% [wt/vol] iodixanol, STEMCELL Technologies, Cat#07820) velocity gradient. Iodixanol gradients were prepared in PBS in 1.2% increments ranging from 6 to 18%. Pseudoviruses were layered onto the top of the gradient and centrifuged for 1.5 hours at 200,000 g in an SW41 Ti rotor. Gradient fraction that contained pseudovirus pellet was collected.

Pseudovirus neutralization assay

CHO-ACE2 cells were seeded at a density of 3.2×10^4 cells in 100 μL of complete medium without Geneticin in 96-well Flat Clear Bottom Black Polystyrene TC-treated Microplates (Corning, Cat#3904). Serially diluted IgG or Fab antibodies were incubated in a 96-well flat-bottom cell culture plate (Costar, Cat#3596) with an equal volume of pseudovirus (12 ng of p24) at the final volume of 50 μL at 37°C for one hour, and the mixture was added to the monolayer of pre-seeded CHO-ACE2 cells in triplicate. After one hour of pseudovirus infection at 37°C, 150 μL of culture medium was added to each well and the cells were further incubated for another 48 hours. Upon removal of culture medium, cells were washed twice with sterile PBS, and then lysed in 20 μL of 1x Passive lysis buffer (Promega, Cat#E1941) with gentle shaking at 37°C for 30 minutes. Luciferase activity was then assessed using a Luciferase Assay System (Promega, Cat#E1510) on a Promega GloMax Luminometer. The relative luciferase units (RLU) were converted to percent neutralization and plotted with a non-linear regression curve fit using GraphPad PRISM.

Live virus neutralization assay in Vero E6 cells

The potency of the IgG or Fab antibodies were determined in neutralizing live SARS-CoV-2 virus assays. In brief, 25 μL of 100 TCID50 of SARS-CoV-2 live virus (isolated from a nasopharyngeal swab of a patient in Singapore) was mixed with an equal volume of serially diluted IgG or Fab antibodies and incubated at 37°C for one hour before the mixture was added to 50 μL of Vero E6 C1008 cells in suspension. The infected cells were incubated at 37°C incubator for four days and the cell viability was determined using Viral Tox-GloTM Assay (Promega, Cat#G8941). The potency of 2H4, 3D11 and 5A6 IgG antibodies in neutralizing live SARS-CoV-2 virus assays was also determined by measuring the viral genome copy number (GCN). 25 μL of 100 TCID50 of SARS-CoV-2 live virus (isolated from a nasopharyngeal swab of a patient in Singapore) was mixed with an equal volume of serially diluted 2H4, 3D11 or 5A6 IgG antibodies and incubated at 37°C for one hour before the mixture was added to 50 μL of 4×10^5 Vero E6 C1008 cells in suspension. The infected cells were incubated at 37°C incubator for 48 hr after which supernatant was harvested and viral GCN was determined by subsequent RT-qPCR targeting the N gene using the RESOLUTE 2.0 kit as per manufacturer's instructions. Briefly, 2.5 μL of supernatant was diluted with 2.5 μL of Milli-Q water and added to 20 μL of RT-PCR master mix. PCR was carried out as follows: reverse transcription at 55°C for 15min, inactivation at 95°C for 4min, followed by 45 cycles of amplification consisting of denaturation at 95°C for 3 s and annealing/extension at 62°C for 30 s and GCN values determined by comparing Ct values against a logGCN standard curve.

Live virus neutralization assay in HAE

The potency of 5A6 IgG was tested in neutralizing a live virus strain (BetaCoV/France/IDF0571/2020) using MucilAirTM HAE (human airway epithelia) model. Briefly, the apical poles of HAE were gently washed twice with warm Opti-MEM medium (GIBCO, Thermo Fisher Scientific) and then infected directly with a 150 μL dilution of live SARS-CoV-2 virus strain (BetaCoV/France/IDF0571/2020) in Opti-MEM medium, at a multiplicity of infection (MOI) of 0.1. Viral suspensions were pre-incubated for 60 min with antibody 5A6 IgG (75 ng/ml or 150 ng/ml) or an anti-Ebola glycoprotein control antibody (150 ng/ml) before infection. A control infection was performed in absence of antibody. For mock infection, the same procedure was followed using Opti-MEM as inoculum. Viral replication was quantified as the measured copy number of the viral genomes inside, and at the apical poles of, nasal and bronchial HAE. Samples collected from apical washes at 48 hours post-infection were separated into 2 tubes: one for TCID50 viral titration (stored at -80°C) and one for RT-qPCR. HAE cells were harvested in RLT buffer (QIAGEN) and total RNA was extracted using the RNeasy Mini Kit (QIAGEN) for subsequent RT-qPCR. Primer and probe sequences targeting the ORF1b-nsp14 (forward primer HKU-ORF1b-nsp14F: 5'-TGGGGYTTTACRGGTAACCT-3'; reverse primer HKU-ORF1b-nsp14R: 5'-AACRCGCTTAACAAAGCACTC-3'; probe HKU-ORF1b-nsp141P: 5'-FAM-TAGTTGTGATGCWATCATGACTAG-TAMRA-3') were selected from those designed by the School of Public Health/University of Hong Kong (Leo Poon, Daniel Chu and Malik Peiris) and synthesized by Eurogentec. Real-time one-step RT-qPCR was performed using the EXPRESS One-Step Superscript qRT-PCR Kit (Invitrogen, Cat#1178101K). Variations in *trans* epithelial electrical resistance (ΔTEER) were measured using a dedicated volt-ohm meter (EVOM2, Epithelial Volt/Ohm Meter for TEER) and expressed as Ohm/cm².

Cell-cell fusion assay

Vero E6 cells were transfected with S protein bearing furin recognition mutation (R682RAR to A682AAR) with C-terminal GFP tag by Lipofectamin 2000 (Invitrogen) and were cultured on μ -Slide 8 well chamber slides (Ibidi, Cat#80826). The transfection efficiency was monitored by percentage of GFP positive cells and optimized within 15%–30% to achieve the best signal-to-noise ratio in the following cell-cell fusion assay. After 48 hours, cells were treated with various antibodies diluted in DMEM without FBS for 1 hour at 37°C. Cells were then treated with 15 $\mu\text{g}/\text{ml}$ trypsin and incubated at 37°C for another 2 hours. After trypsin treatment, cells were fixed with 4% PFA at room temperature for 15 mins and the cell nuclei were stained with DAPI. Images were taken by Olympus confocal microscope.

Fab affinity measurement by BLI

Binding affinity of purified Fab to RBD was measured on the Octet96Red system (ForteBio). Anti-human IgG Fc (AHC) sensors were first loaded with 1 $\mu\text{g}/\text{ml}$ of Fc-RBD for 10 min, followed by kinetics buffer (phosphate-buffered saline buffer supplemented with 0.1% Tween-20 and 0.1% BSA) for 5 min to establish a stable baseline. The sensors were then dipped into different concentrations of each Fab from 100 nM to 3.125 nM in two-fold dilutions for 6 min, and then in kinetics buffer again for 10 min to measure association and

dissociation. Assays were run at 25°C and data was analyzed on the Octet System Data Acquisition Software version 9.0.0.4. using the 1:1 Langmuir binding model.

Avidity binding by BLI

Avidity of anti-SARS-CoV-2 Spike RBD IgG antibodies for RBD was measured on the Octet96Red system. Anti-IgG Fc capture (AHC) sensors were used. The sensors were loaded with 1 µg/ml of Fc-RBD (made in-house) in assay buffer (phosphate-buffered saline buffer supplemented with 0.1% Tween-20 and 0.1% BSA) for 10 min, quenched in 0.5 mg/ml of isotype IgG in assay buffer for 10 min, then dipped in assay buffer for 12 min for the system to stabilize. To measure the association of 5A6, the sensors were dipped in a range of 5A6 IgG concentrations (25–0.39 nM in 2-fold serial dilutions) in assay buffer for 6 min. To measure dissociation, the sensors were dipped in assay buffer for 10 min. The experiment was conducted at 25°C. Data analysis was done in the Octet System Data Acquisition Software version 9.0.0.4. using the 1:2 bivalent model.

Epitope binning by BLI

Epitope binning was done using a classical sandwich assay. The AR2G sensor tips (ForteBio) were activated in freshly prepared 20mM EDC (1-ethyl-3-[3-dimethylaminopropyl]-carbodiimide hydrochloride), 10mM NHS (N-hydroxysuccinimide) solution and the 5A6 antibody was immobilized to the sensor tips using a concentration of 7.5 µg/ml of 5A6 in 10 mM sodium acetate pH 6 buffer. After quenching in 1M ethanolamine, the 5A6-immobilized sensor tips were dipped in 5 µg/ml of tagless RBD for 600 s, then in 10µg/ml of the second antibody for 300 s. The assay was run at 25°C. Sensor tips were regenerated in 10 mM glycine at pH 2.7 and neutralized in PBS with 0.1% Tween-20 before another cycle of sandwich assay was performed. Each sensor tip was used in a total of 3 cycles. Data analysis was done in the Octet System Data Acquisition Software version 9.0.0.4.

IgG and Fab affinity for Spike trimer by SPR

StreptagII-tagged prefusion S ectodomain, diluted to 10 µg/mL in 10 mM HEPES, 150 mM NaCl, 3 mM EDTA, 0.05% PS-20, pH 7.4, was captured on a StreptactinXT-immobilized (Iba Life Sciences) CM5 Series S sensor chip at an average level of 224 or 347 RU (response units) for IgG and Fab kinetics measurements, respectively using a Biacore T200 (Cytiva Life Sciences). 2-fold serial dilutions of purified IgG from 12.5 nM to 0.39 nM or Fab from 100 nM to 3.125 nM were flowed over the captured prefusion S ectodomain at 30 µL/minute for 90 s followed by 420 s of dissociation flow. Following each cycle, the chip surface was regenerated with 3 M guanidine hydrochloride. The resulting reference flow cell and blank-injection subtracted sensorgrams were fit to a 1:1 Langmuir binding model using the Biacore T200 Evaluation Software (Cytiva Life Sciences).

Statistical analysis

Data were analyzed using GraphPad Prism version 7.03. Statistical tests are indicated in the figure legends. EC₅₀ values were calculated by non-linear regression analysis on the binding curves using GraphPad Prism and IC₅₀ values were calculated either using the [Inhibitor] versus response variable slope four parameter non-linear regression model of GraphPad Prism, or the four parameter logistic regression model in the Quest Graph IC₅₀ Calculator from AAT Bioquest, Inc (<https://www.aatbio.com/tools/ic50-calculator>). One-way analysis of variance (ANOVA) was used to compare differences between groups. Differences were considered statistically significant at confidence levels *p < 0.05 or **p < 0.01, ***p < 0.001.

Supplemental figures

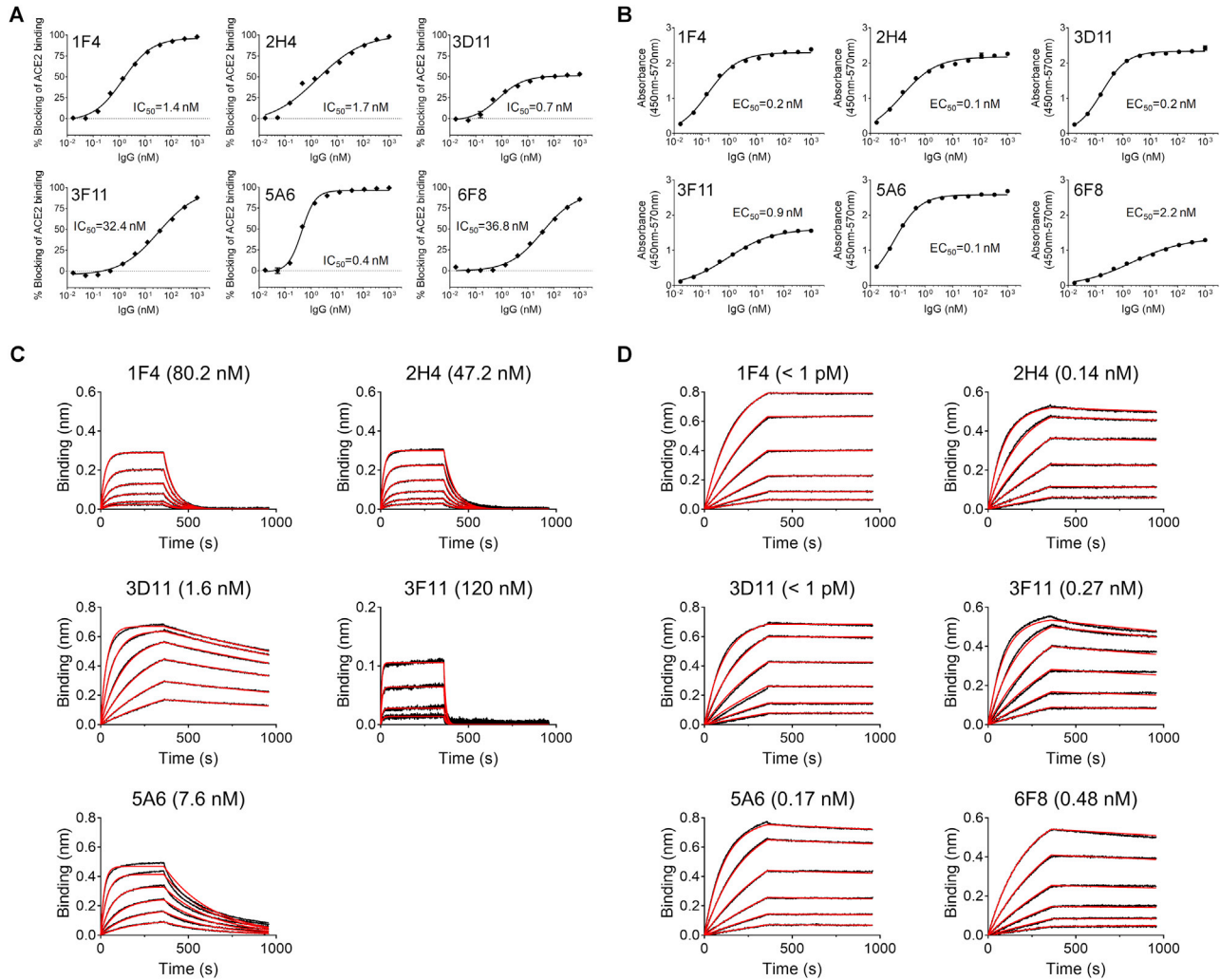


Figure S1. Characterization of SARS-CoV-2 receptor-blocking antibodies, related to Figure 1

(A) Blocking of ACE2/SARS-CoV-2 RBD interaction by 1F4, 2H4, 3D11, 3F11, 5A6 and 6F8 IgGs tested by competition ELISA. Data are presented as mean \pm SD in triplicates and are representative of two independent experiments. (B) Binding avidity of 1F4, 2H4, 3D11, 3F11, 5A6 and 6F8 IgG antibodies to SARS-CoV-2 Spike RBD proteins tested by ELISA. Data are presented as mean \pm SD in triplicates and are representative of two independent experiments. (C) Binding affinity of five Fab clones to SARS-CoV-2 Spike RBD protein measured by biolayer interferometry. Fab binding to immobilized Fc-RBD was tested using a range of Fab concentrations from 100 nM to 3.125 nM (in 2-fold dilution). A representative set of measurements from two independent experiments is shown with sensorgrams in black and curve fittings in red. (D) Binding avidity of six IgGs to the RBD by biolayer interferometry. IgG Binding to immobilized Fc-RBD was tested using a range of IgG concentrations from 12.5 nM to 0.39 nM (in 2-fold dilutions). The anti-Fc sensor chip was quenched with excess irrelevant, same-isotype IgG to prevent confounding from antibody binding directly to the chip. A representative set of measurements from two independent experiments is shown with sensorgrams in black and curve fittings in red.

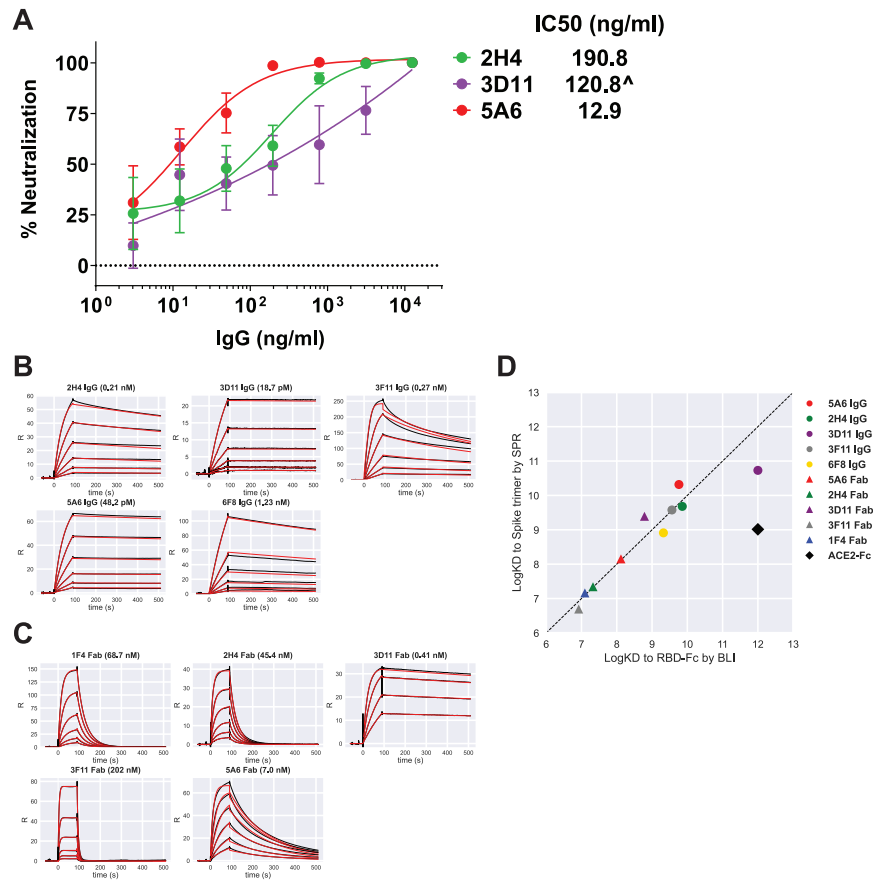


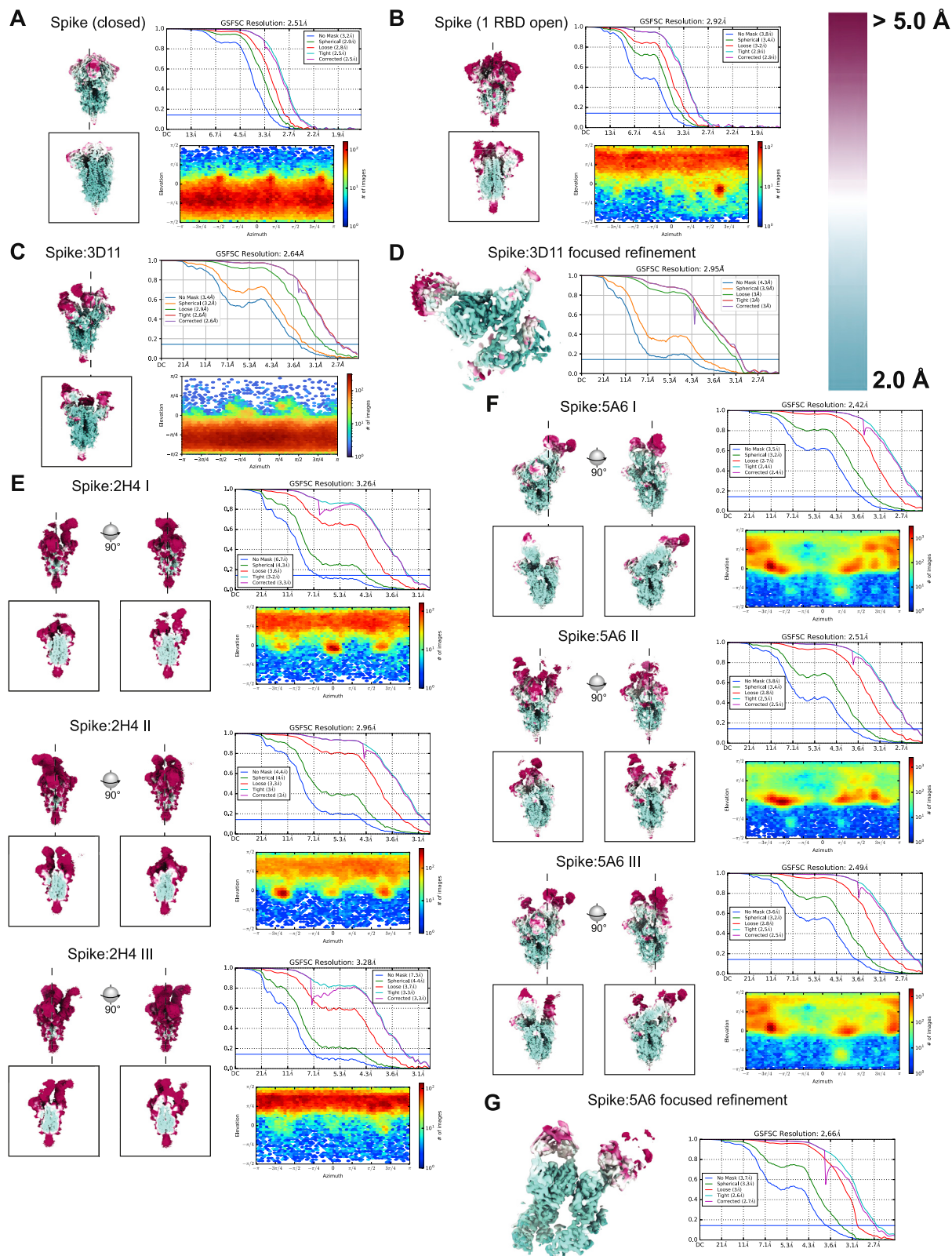
Figure S2. SARS-CoV-2 live virus neutralization and antibody binding to the Spike trimer measured by SPR, related to Figure 2

(A) The potency of 2H4, 3D11 and 5A6 IgG antibodies in neutralizing live SARS-CoV-2 virus assays determined by measuring the viral genome copy number (GCN). Infection of Vero E6 C1008 cells by SARS-CoV-2 live virus (isolated from a nasopharyngeal swab of a patient in Singapore) were determined in the presence of receptor blocking IgGs 2H4, 3D11 and 5A6. 48 hours post infection, culture supernatant was harvested and viral GCN was determined by RT-qPCR targeting the N gene and GCN values were determined by comparing Ct values against a logGCN standard curve. The GCN values were then converted to percent neutralization and plotted with a non-linear regression curve fit using PRISM. IC₅₀ was calculated by a variable slope four parameter non-linear regression model in Graphpad PRISM 7 without or with top and bottom constraints set at 100% and 0% respectively. Data are presented as mean ± SEM from 6 replicates.

(B) Binding avidity of IgG clones 2H4, 3D11, 3F11, 5A6, and 6F8 for intact Spike trimer measured by surface plasmon resonance (SPR). A range of IgG concentrations from 12.5 nM to 0.39 nM (in 2-fold serial dilution) are shown, with sensorgrams in black and curve fits in red.

(C) Binding affinity of Fab clones 1F4, 2H4, 3D11, 3F11, and 5A6 for intact Spike trimer measured by surface plasmon resonance (SPR). A range of Fab concentrations from 100 nM to 3.125 nM (in 2-fold serial dilution) are shown, with sensorgrams in black and curve fits in red.

(D) Log-log scatterplot comparing antibody binding constants for Fc-RBD (x axis) to those for Spike trimer (y axis). Affinity or avidity of antibodies or Fab fragments for the flexible Fc-RBD construct represent binding without geometric constraints, while measurements using immobilized Spike trimers represent binding with the specific geometries afforded by the Spike:antibody complexes. For most species, SPR and BLI measurements are similar, however 3D11 IgG and ACE2-Fc bind significantly more weakly to relatively unrestricted Fc-RBD than to Spike trimer (note that the 3D11 IgG binds > 10x more tightly than 3D11 Fab in both sets of experiments, indicating avid binding). 5A6 IgG binds somewhat more tightly to Spike trimer than to Fc-RBD, perhaps indicating that RBDs within a Spike trimer have particularly favorable geometries for binding.

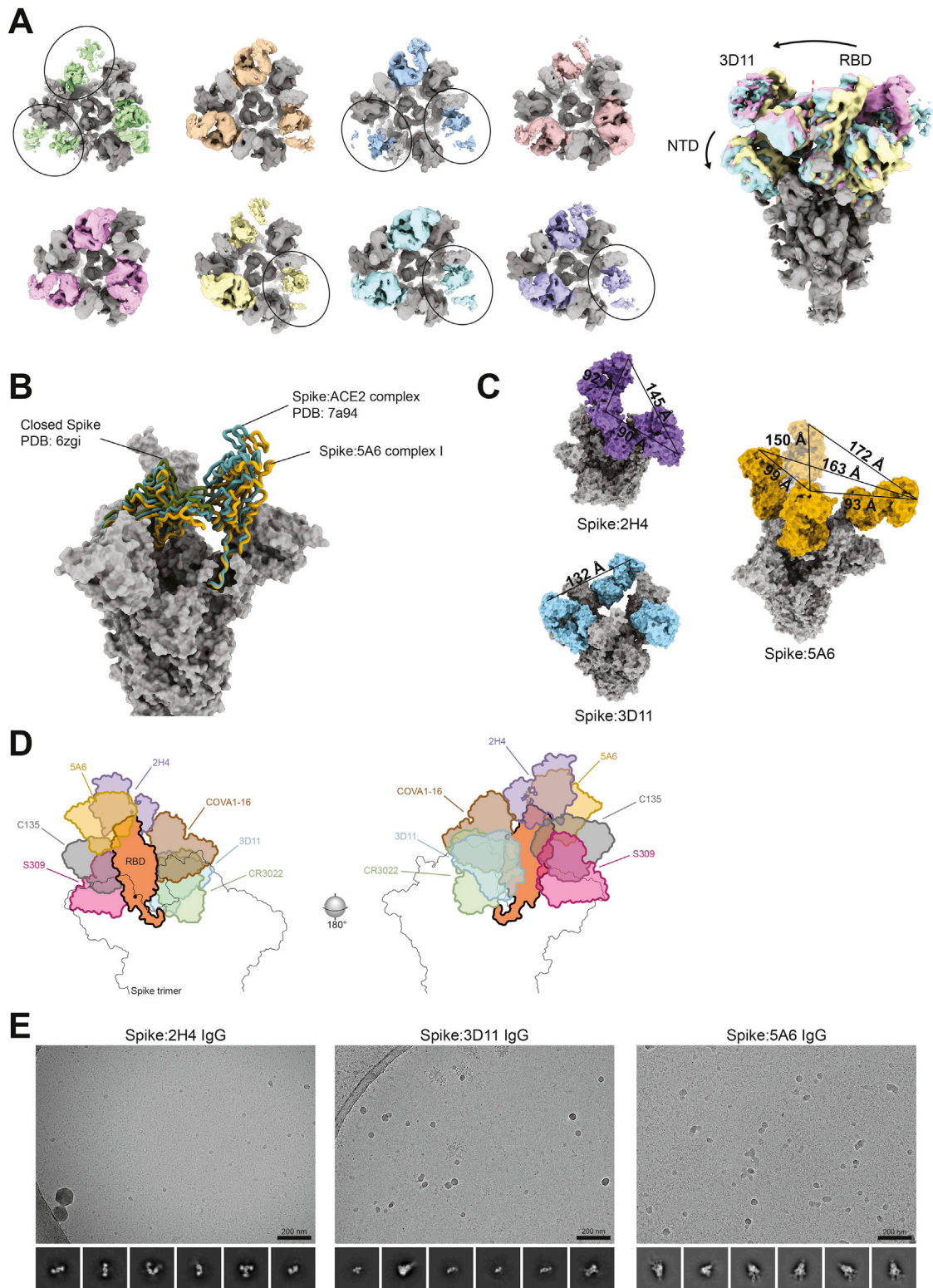


(legend on next page)

Figure S3. Cryo-EM densities and resolution estimation, related to Figure 4

Density maps colored by local resolution, Fourier shell correlation curves, and particle orientation distributions for the structures reported in this work. All maps use the same local resolution scale, shown at the top right of the figure.

- (A) The apo Spike, with all RBDs closed.
- (B) The apo Spike, with one RBD open.
- (C) The Spike:3D11 complex.
- (D) Refinement of Spike:3D11, focused on the Fab variable domains and RBD epitope.
- (E) Spike:2H4 complexes with one, two, or three Fabs bound.
- (F) Spike:5A6 complexes.
- (G) Refinement of Spike:5A6 complex I, focused on the Fab variable domains and quaternary epitope involving two RBDs (one open, with the clockwise adjacent RBD trapped closed).



(legend on next page)

Figure S4. Additional structural details, related to Figure 4

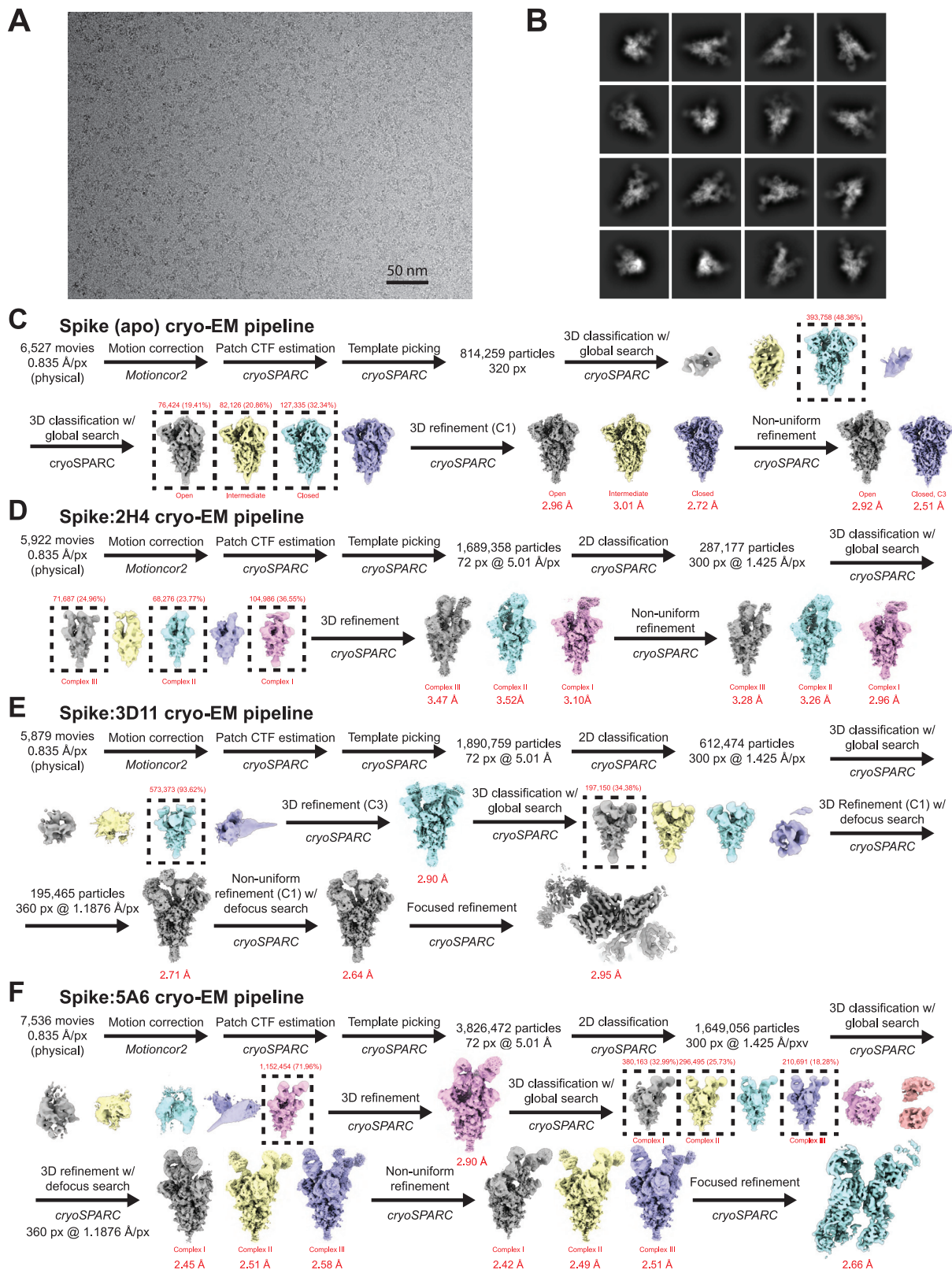
(A) Eight subclasses of the Spike:3D11 complex, determined using symmetry relaxation in Relion 3.1. At left, top views show that these classes vary in the occupancy of Fab at each RBD. Only Fabs are colored, with missing or weak Fab densities are indicated by black ellipses. At right, two extremum classes and one intermediate show relative motion of the RBDs and NTDs, relaxations which likely contribute to the S2 unsheathing that eventually permits Spike-mediated membrane fusion. Fabs, RBDs, and NTDs are colored, and a dashed line delineates Fab and RBD. The general direction of S2-opening movements, as observed in the classes, are indicated by black arrows.

(B) The quaternary epitope bound by 5A6 is cryptic because the Fab stabilizes unique conformations of RBDs, observed only in the complex, that contribute to the epitope. RBDs from Spike:5A6 complex I (goldenrod) are shown relative to the fully closed Spike (PDB: 6zgi, forest green) and to the Spike with one RBD open and bound to ACE2 (PDB: 7a94, cadet blue). Interestingly, the open RBD bound to 5A6 is more open than that bound to ACE2, yet the neighboring RBD trapped closed by 5A6 is more closed than in the singular ACE2 complex or the fully closed Spike.

(C) The hinge regions connecting the Fc domain of an IgG antibody to each of its two Fabs are 23 residues long, approximately 10 of which are flexible due to disulfide bonds. Assuming a standard polypeptide length of about 3.5 Å per residue, each hinge might extend as far as 35 Å, allowing for some 70 Å separation between the two Fabs. As shown, the shortest gaps between Fabs in the Spike:2H4 and Spike:5A6 complexes are ~90 Å, however variation of the elbow angles between Fab V and C domains could reduce the effective separation. Different Fab clones have elbow angles across just over 90° (Stanfield et al., 2006), and changes as great as 37° have been observed between multiple structures of the same clone (Wilson and Stanfield, 1994). For example, a 15° elbow bend might reduce separation by 10 Å at each Fab (20 Å total), to about the maximum length of the hinge. Bivalent, IgG-bound states thus likely differ in Fab elbow angle and feature some relaxation of the RBDs, in order to support the avid binding of IgG antibodies to Spike trimer observed in our experiments.

(D) Comparison of 2H4, 3D11, and 5A6 to non-receptor binding motif antibodies reported in literature. The 2D representation of molecular surface models, with superposed RBDs, shows that C135 and S309 bind to the outward face of the RBD, which is exposed in the closed state, while our antibodies 5A6 and 2H4 bind to the tip of the RBD at epitopes that partially overlap the RBS. Finally, COVA1-16, CR3022, and our 3D11 clone all bind to the inward face of the RBD, which is hidden in the closed state. These last three have overlapping epitopes, but different binding geometries such that, unlike COVA1-16 and 3D11, CR3022 actually clashes severely with the NTD even when the bound RBD is open.

(E) Example cryo-EM images and selected 2D class averages for Spike incubated with 2H4 IgG (left), 3D11 IgG (center), or 5A6 IgG (right). Images were collected on a Talos Arctica at 200 keV and low-pass filtered to 20 Å. The Spike:2H4 IgG sample contains numerous, relatively small particles, and some of its 2D class averages resemble monomeric Spike (classes 4 and 6) or two Spike monomers crosslinked by antibody (class 3). In the Spike:3D11 IgG sample, much of the protein is contained within stereotypical aggregates approximately 150 nm in size. Notable 2D averages resemble a Fab bound to Spike RBD (classes 3-5), rare Spike trimers in the closed conformation (class 2), and a potential Spike dimer or pair of monomers crosslinked by antibody (class 6). In contrast to the others, Spike:5A6 IgG is a well behaved sample (despite the crowded micrograph). The 2D class averages are easily recognizable as intact Spike trimer, as is the unique binding mode of 5A6.



(legend on next page)

Figure S5. Cryo-EM processing, related to Figure 4

- (A) A micrograph drawn from the Spike:5A6 complex dataset, representative of those obtained for the Fab complexes.
- (B) Selected 2D class averages of Spike:5A6 particles, evincing clear secondary structure and multiple Fabs bound to the RBDs.
- (C) Cryo-EM image processing workflow for Spike alone, leading to structures of the trimer with all RBDs closed, and with one RBD open or in an intermediate state.
- (D) Processing workflow for the Spike:2H4 complex, resulting in structures with one, two, or three Fabs bound, as presented in the text.
- (E) Processing workflow for the Spike:3D11 complex, culminating in a high-resolution structure of the Fab and RBD epitope.
- (F) Processing workflow for the Spike:5A6 complex, resulting in the complexes presented in the text. Note the fourth class found during the second 3D classification step is a lower resolution duplicate of Spike:5A6 complex III. Processing culminates in a high-resolution of the Fab and its quaternary epitope involving two RBDs.

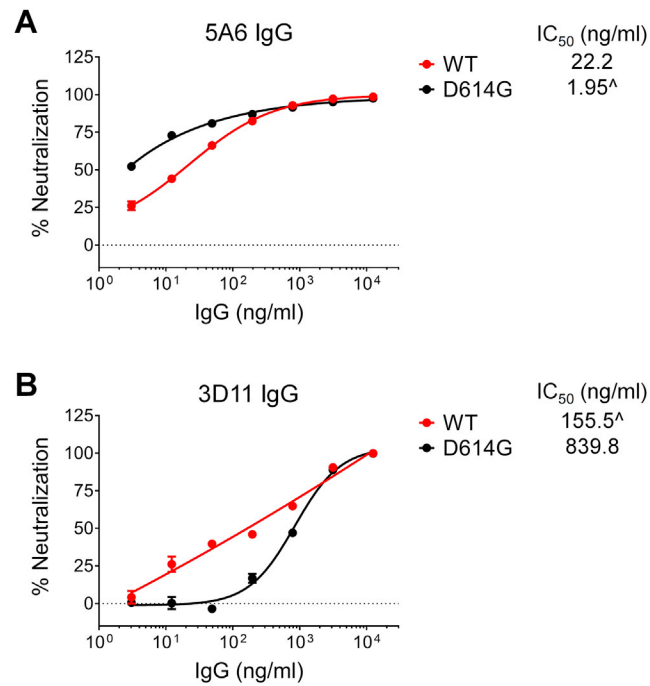


Figure S6. Neutralization of the SARS-CoV-2 pseudovirus with Spike mutant D614G, related to Figure 6

(A) Neutralization by 5A6 of SARS-CoV-2 pseudovirus bearing either wild-type Spike protein (red), or Spike with the D614G mutation (black). The efficacy of 5A6 IgG is against D614G mutant Spike is improved over wild-type.

(B) Neutralization by 3D11 of SARS-CoV-2 pseudovirus bearing either wild-type Spike protein (red), or Spike with the D614G mutation (black). 3D11 IgG suffers a severe loss of efficacy against the mutant pseudovirus (more than 5-fold weaker IC₅₀). Data are presented as mean ± SEM in triplicates and are representative of two independent experiments. IC₅₀ was calculated by variable slope four parameter non-linear regression model using Graphpad PRISM 7 Software without or with top and bottom constraints set at 100% and 0% respectively.